

## Article

# Enhanced Catalytic Performance and Sulfur Dioxide Resistance of Reduced Graphene Oxide-Promoted MnO<sub>2</sub> Nanorods-Supported Pt Nanoparticles for Benzene Oxidation

Dan Zhang<sup>1</sup>, Qing Ye<sup>1,\*</sup> , Ning Dong<sup>1,2</sup>, Wenjin Wang<sup>1</sup>, Yang Xiao<sup>1</sup> and Hongxing Dai<sup>3,\*</sup>

<sup>1</sup> Key Laboratory of Beijing on Regional Air Pollution Control, Department of Environmental Science, Faculty of Environment and Life, Beijing University of Technology, Beijing 100124, China

<sup>2</sup> Beijing Huaneng Yangtze Environmental Technology Research Institute Co., Ltd., Beijing 102209, China

<sup>3</sup> Beijing Key Laboratory for Green Catalysis and Separation, Key Laboratory of Beijing on Regional Air Pollution Control, Key Laboratory of Advanced Functional Materials, Education Ministry of China, and Laboratory of Catalysis Chemistry and Nanoscience, Department of Chemical Engineering, Faculty of Environment and Life, Beijing University of Technology, Beijing 100124, China

\* Correspondence: yeqing@bjut.edu.cn (Q.Y.); hxdai@bjut.edu.cn (H.D.); Tel.: +86-10-6739-1659 (Q.Y.); +86-10-6739-6118 (H.D.); Fax: +86-10-6739-1983 (Q.Y. & H.D.)

**Abstract:** The reduced graphene oxide (rGO)-promoted  $\alpha$ -MnO<sub>2</sub> nanorods-supported Pt ( $x$ Pt- $y$ rGO/ $\alpha$ -MnO<sub>2</sub>,  $x = 0.93$  wt%,  $y = 0.5, 1.0,$  and  $2.0$  wt%) nanocatalysts were prepared using a polyvinyl alcohol (PVA)-protected reduction method. After an appropriate loading of Pt on  $\alpha$ -MnO<sub>2</sub>, the strong metal-support interaction between Pt and  $\alpha$ -MnO<sub>2</sub> was beneficial for an increase in catalytic activity. The simultaneous addition of rGO to  $\alpha$ -MnO<sub>2</sub> not only provided a more amount of benzene adsorption sites, but also acted as an electron transfer channel to accelerate charge migration, thus further improving catalytic activity of  $\alpha$ -MnO<sub>2</sub>. Among all of the catalyst samples, 0.94Pt-1.0rGO/ $\alpha$ -MnO<sub>2</sub> showed the best catalytic performance with 90% benzene conversion at 160 °C and a gas hourly space velocity (GHSV) of 60,000 mL/(g h), which was better than that over the other Pt-based catalysts. The results of in situ DRIFTS characterization revealed that phenol, benzoquinone, and carboxylate species were the intermediates and eventually oxidized to CO<sub>2</sub> and H<sub>2</sub>O. When sulfur dioxide was present, catalytic activity of  $\alpha$ -MnO<sub>2</sub> decreased due to the formation of manganese sulfate that blocked the active sites, while the loading of Pt and rGO hindered the chemisorption of SO<sub>2</sub> and prevented the active sites of the catalyst from being poisoned by SO<sub>2</sub>, thus enhancing sulfur resistance of the catalyst. The 0.94Pt-1.0rGO/ $\alpha$ -MnO<sub>2</sub> catalyst presented in this work can be considered as a cost-effective and promising catalyst for the oxidative removal of volatile organic compounds.

**Keywords:** volatile organic compound; benzene oxidation; manganese dioxide nanorod; reduced graphene oxide; supported Pt nanocatalyst; sulfur dioxide resistance



**Citation:** Zhang, D.; Ye, Q.; Dong, N.; Wang, W.; Xiao, Y.; Dai, H. Enhanced Catalytic Performance and Sulfur Dioxide Resistance of Reduced Graphene Oxide-Promoted MnO<sub>2</sub> Nanorods-Supported Pt Nanoparticles for Benzene Oxidation. *Catalysts* **2022**, *12*, 1426. <https://doi.org/10.3390/catal12111426>

Academic Editor: Bishweshwar Pant

Received: 13 October 2022

Accepted: 11 November 2022

Published: 13 November 2022

**Publisher's Note:** MDPI stays neutral with regard to jurisdictional claims in published maps and institutional affiliations.



**Copyright:** © 2022 by the authors. Licensee MDPI, Basel, Switzerland. This article is an open access article distributed under the terms and conditions of the Creative Commons Attribution (CC BY) license (<https://creativecommons.org/licenses/by/4.0/>).

## 1. Introduction

Volatile organic compounds (VOCs) are involved in atmospheric photochemical reactions and are also key precursors of PM<sub>2.5</sub> and O<sub>3</sub>, which are prone to photochemical pollution and urban haze [1]. VOCs usually include benzene, toluene, formaldehyde, and etc. These organics can enter human body through the respiratory system and skin, pose a serious threat to human health, and even induce cancer [2,3]. Currently, the main technologies of VOCs treatments include physical adsorption, catalytic oxidation, and biological treatment. Among them, catalytic oxidation is more effective in removing VOCs because of its good safety, no secondary pollution, and low reaction temperatures [4].

At present, the catalysts used for catalytic oxidation mainly include transition metal oxide catalysts and noble metal-based catalysts. Noble metal catalysts show good activity, but their disadvantages are high cost and complicated preparation processes. Although catalytic activities

of transition metal oxides are worse than those of noble metals, the former is cheap and contains a large amount of oxidation state metal ions and lattice defects (oxygen vacancies) and can be used as catalytic supports [5]. Among transition metal oxides, manganese oxides have a variety of valence states, crystal phases, morphologies, and high catalytic oxidation activity, and hence are widely studied in catalytic oxidation of VOCs [6]. For example, Fan et al. [7] successfully synthesized  $\alpha$ -,  $\gamma$ -, and  $\beta$ - $\text{MnO}_2$ , and found that  $\alpha$ - $\text{MnO}_2$  catalyzed toluene oxidation with the best activity due to its good redox performance and high lattice oxygen mobility. Surface metal modification of manganese oxides can improve catalytic performance. Using manganese oxides as a support and doping noble metals or transition metals in appropriate amounts can increase the oxygen vacancies and improve catalytic oxidation activity and thermal stability of the catalysts. The impact of Cu-doped  $\text{MnO}_2$  on the removal efficiency of two ketones VOCs was investigated by Zeng et al. [8] The synergistic interaction between Cu and Mn in the Cu-Mn catalysts was found to improve the catalytic activity by increasing the surface active oxygen concentration and low-temperature reducibility. Huang et al. [9] studied the formaldehyde oxidation over the Ag/ $\text{MnO}_2$  nanorods with different silver loadings, and observed that 0.1% Ag/ $\text{MnO}_2$ -r could catalyze the complete conversion of HCHO at 80 °C. The increase in catalytic activity was attributed to the strong metal-support interaction (SMSI), increased surface oxygen vacancies, and improved surface lattice oxygen mobility of  $\text{MnO}_2$ , and enhanced low-temperature reducibility.

Graphene oxide (GO) is widely used in heterogeneous catalysis because of its unique two-dimensional layered structure, high surface area, and powerful electron transport ability. In recent years, there have been several studies on improving the efficiency of catalysts for catalytic oxidation of CO and VOCs by doping with graphene. Reduced graphene oxide (RGO) was introduced into the Au/3DOM  $\text{Co}_3\text{O}_4$  catalysts by Xie et al. [10] to obtain a series of Au/rGO/3DOM  $\text{Co}_3\text{O}_4$  catalysts. It was shown that rGO acted as an electron transmission channel between Au and 3DOM  $\text{Co}_3\text{O}_4$ , and significantly enhanced the SMSI and the activation of oxygen molecules, hence resulting in a significant improvement in catalytic CO oxidation activity. Lu et al. [11] loaded GO on  $\text{MnO}_2$ , and found that the loading of GO gave rise to a complete conversion of HCHO in HCHO oxidation at 65 °C.

In this work, we adopted the polyvinyl alcohol (PVA)-protecting reduction strategy to prepare the  $x\text{Pt-yrGO}/\alpha\text{-MnO}_2$  catalysts, employed various techniques to characterize their physicochemical properties, evaluated their catalytic activities for benzene oxidation, examined their water and sulfur dioxide resistance, and investigated their reaction mechanisms.

## 2. Results and Discussion

### 2.1. Catalyst Performance and Stability

#### 2.1.1. Catalyst Performance

Figure 1A shows the catalytic activities of  $x\text{Pt-yrGO}/\alpha\text{-MnO}_2$  ( $x = 0.93\text{--}0.95$  wt%,  $y = 0.5, 1.0$ , and  $2.0$  wt%) samples for benzene oxidation, and their  $T_{10\%}$ ,  $T_{50\%}$ , and  $T_{90\%}$  values are summarized in Table 1. At a GHSV of 60,000 mL/(g h), catalytic activity decreased in the order of  $0.94\text{Pt-1.0rGO}/\alpha\text{-MnO}_2$  ( $T_{90\%} = 169$  °C) >  $0.92\text{Pt-2.0rGO}/\alpha\text{-MnO}_2$  ( $T_{90\%} = 178$  °C) >  $0.91\text{Pt-0.5rGO}/\alpha\text{-MnO}_2$  ( $T_{90\%} = 188$  °C) >  $0.93\text{Pt}/\alpha\text{-MnO}_2$  ( $T_{90\%} = 205$  °C) >  $\alpha\text{-MnO}_2$  ( $T_{90\%} = 300$  °C). The performance of the  $x\text{Pt-yrGO}/\alpha\text{-MnO}_2$  samples was significantly higher than that of the  $\alpha\text{-MnO}_2$  and rGO-free  $0.93\text{Pt}/\alpha\text{-MnO}_2$  samples. For example, the  $T_{50\%}$  and  $T_{90\%}$  over  $0.94\text{Pt-1.0rGO}/\alpha\text{-MnO}_2$  were 163 and 169 °C, while those over rGO-free  $0.93\text{Pt}/\alpha\text{-MnO}_2$  were 190 and 205 °C, respectively. In addition, different loadings of rGO led to a difference in catalytic activity. The activity of  $x\text{Pt-yrGO}/\alpha\text{-MnO}_2$  increased with the rise in rGO loading from 0.5 to 1.0 wt%, but decreased when the rGO loading rose from 1.0 to 2.0 wt%. This result might be due to the partial covering of the surface active sites on the catalyst by the excessively loaded rGO. Among all of the samples,  $0.94\text{Pt-1rGO}/\alpha\text{-MnO}_2$  showed the highest catalytic activity, which was associated with the

loading of rGO, the promotion of the electron transfer between Pt and  $\alpha$ -MnO<sub>2</sub>, and the enhancement of the SMSI between Pt and  $\alpha$ -MnO<sub>2</sub> [12].

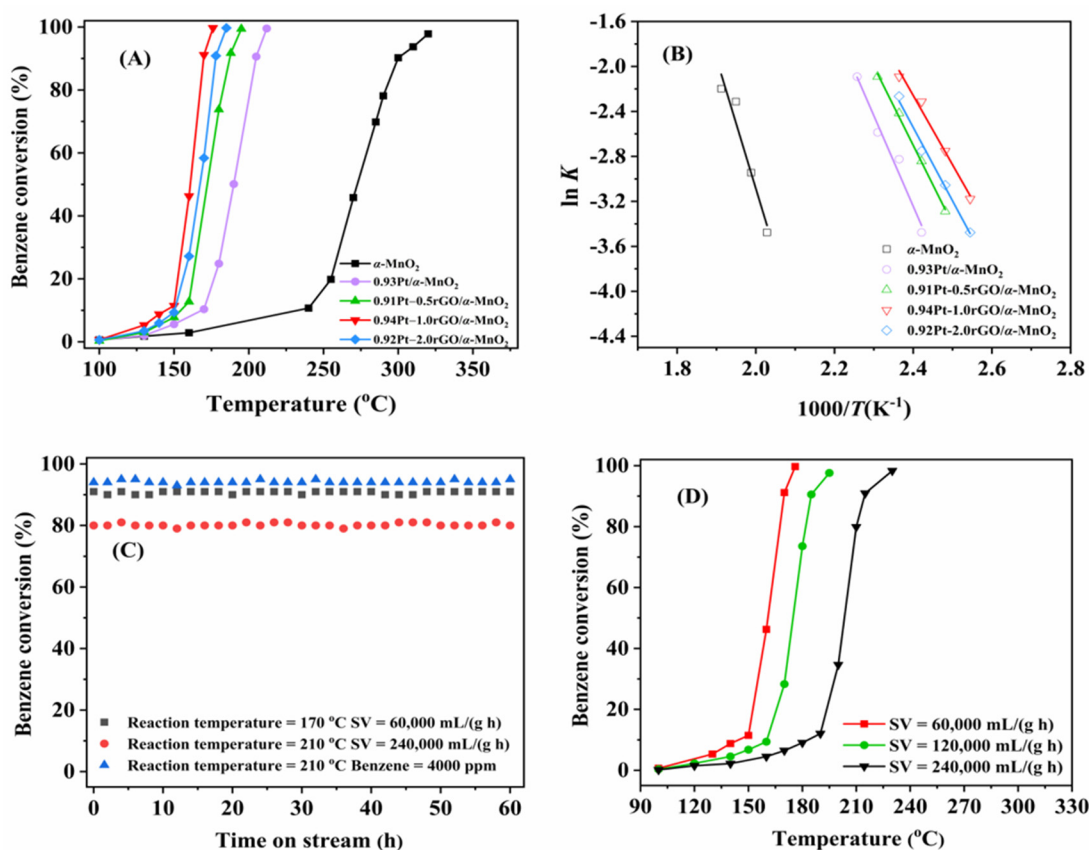


**Figure 1.** (A) Benzene conversion as a function of temperature, (B) Arrhenius plots for the oxidation of benzene over the  $\alpha$ -MnO<sub>2</sub> and xPt-yrGO/ $\alpha$ -MnO<sub>2</sub> samples at SV = 60,000 mL/(g h), (C) catalytic stability of 0.94Pt-1.0rGO/ $\alpha$ -MnO<sub>2</sub> under different conditions, and (D) effect of GHSV on catalytic activity of 0.94Pt-1.0rGO/ $\alpha$ -MnO<sub>2</sub> at benzene concentration = 1000 ppm.

**Table 1.** Catalytic activities, apparent activation energies ( $E_a$ ), TOF<sub>Pt</sub> at 149 °C, and specific reaction rates at 149 °C ( $r_{cat}$ ) of the  $\alpha$ -MnO<sub>2</sub> and xPt-yrGO/ $\alpha$ -MnO<sub>2</sub> samples at GHSV = 60,000 mL/(g h).

Sample	Benzene Oxidation Activity			$E_a$ (kJ/mol)	TOF <sub>Pt</sub> ( $\times 10^{-2}$ s <sup>-1</sup> )	$r_{cat}$ (mol/(g s))
	$T_{10\%}$ (°C)	$T_{50\%}$ (°C)	$T_{90\%}$ (°C)			
$\alpha$ -MnO <sub>2</sub>	240	275	300	96.1	—	$1.91 \times 10^{-5}$
0.93Pt/ $\alpha$ -MnO <sub>2</sub>	170	190	205	67.0	0.28	$5.11 \times 10^{-5}$
0.91Pt-0.5rGO/ $\alpha$ -MnO <sub>2</sub>	158	176	188	58.4	0.47	$8.18 \times 10^{-5}$
0.94Pt-1.0rGO/ $\alpha$ -MnO <sub>2</sub>	149	163	169	51.3	1.54	$3.14 \times 10^{-4}$
0.92Pt-2.0rGO/ $\alpha$ -MnO <sub>2</sub>	152	168	178	54.3	0.85	$1.84 \times 10^{-4}$

According to the activity data and the Pt loadings in the samples, their TOFs for benzene oxidation were calculated, as listed in Table 1. The TOFs ( $0.47 \times 10^{-2}$ – $1.54 \times 10^{-2}$  s<sup>-1</sup>) over xPt-yrGO/ $\alpha$ -MnO<sub>2</sub> were significantly higher than that ( $0.28 \times 10^{-2}$  s<sup>-1</sup>) over rGO-free 0.93Pt/ $\alpha$ -MnO<sub>2</sub>. Among all of the samples, 0.94Pt-1.0rGO/ $\alpha$ -MnO<sub>2</sub> exhibited the highest TOF at 149 °C ( $5.73 \times 10^{-2}$  s<sup>-1</sup>). Furthermore, the  $r_{cat}$  values ( $8.18 \times 10^{-5}$ – $3.14 \times 10^{-4}$  mol/(g<sub>Pt</sub> s)) over xPt-yrGO/ $\alpha$ -MnO<sub>2</sub> were higher than that ( $5.11 \times 10^{-5}$  mol/(g<sub>Pt</sub> s)) over 0.93Pt/ $\alpha$ -MnO<sub>2</sub>. Among all of the samples, 0.94Pt-1.0rGO/ $\alpha$ -MnO<sub>2</sub> showed the highest benzene oxidation rate, which was consistent with the sequence in catalytic activity. Moreover, Table S1 summarizes the reaction rates ( $r_{cat}$ ) for benzene oxidation over the different samples

reported in the literature. Obviously, the  $r_{\text{cat}}$  value at 149 °C decreased in the sequence of 0.94Pt-1.0rGO/ $\alpha$ -MnO<sub>2</sub> ( $6.35 \times 10^{-4}$  mol/(g<sub>Pt</sub> s)) [13] > Pt/TMS ( $2.04 \times 10^{-5}$  mol/(g<sub>Pt</sub> s)) [14] > Pt/TS-1 ( $6.82 \times 10^{-5}$  mol/(g<sub>Pt</sub> s)) [14] > Pt/eggshell ( $4.08 \times 10^{-4}$  mol/(g<sub>Pt</sub> s)) [15] > Pt/OMS-2 ( $1.58 \times 10^{-4}$  mol/(g<sub>Pt</sub> s)) [16] > Pt<sub>1</sub>/meso-Fe<sub>2</sub>O<sub>3</sub> ( $6.82 \times 10^{-5}$  mol/(g<sub>Pt</sub> s)) [17].

Many studies [4–9] carried out in recent years have shown that the oxidation of VOCs conforms to a first-order reaction mechanism, so that at a benzene/O<sub>2</sub> molar ratio = 1/400 (excess O<sub>2</sub>), the oxidation of benzene would also follow the first-order reaction mechanism toward benzene concentration ( $c$ ):  $r_{\text{cat}} = -kc = (-A\exp(-E_a/RT)) c$ , where  $k$  is the rate constant (s<sup>-1</sup>),  $A$  is the pre-exponential factor, and  $E_a$  is the apparent activation energy (kJ/mol). Figure 1B shows the Arrhenius plots of benzene oxidation over  $\alpha$ -MnO<sub>2</sub> and  $x$ Pt- $y$ rGO/ $\alpha$ -MnO<sub>2</sub>, and their  $E_a$  values are listed in Table 1. The order of  $E_a$  was:  $\alpha$ -MnO<sub>2</sub> (96.1 kJ/mol) > 0.93Pt/ $\alpha$ -MnO<sub>2</sub> (67.0 kJ/mol) > 0.91Pt-0.5rGO/ $\alpha$ -MnO<sub>2</sub> (58.4 kJ/mol) > 0.92Pt-2.0rGO/ $\alpha$ -MnO<sub>2</sub> (54.3 kJ/mol) > 0.94Pt-1.0rGO/ $\alpha$ -MnO<sub>2</sub> (51.3 kJ/mol). The decrease in  $E_a$  facilitated the oxidation of benzene. Therefore, the oxidation reaction of benzene could take place more readily over the  $x$ Pt- $y$ rGO/ $\alpha$ -MnO<sub>2</sub> samples, as compared with  $\alpha$ -MnO<sub>2</sub>. These results fully indicate that loading rGO on Pt/ $\alpha$ -MnO<sub>2</sub> can significantly improve catalytic activity of benzene oxidation. In addition, compared with the results reported in the literature, we find that the  $E_a$  value decreases in the order of Pt-CeO<sub>2</sub> (400) (75.6 kJ/mol) [18] > Pt-TMS (73.6 kJ/mol) [19] > Pt-WAl<sub>2</sub>O<sub>3</sub>-2 (72.0 kJ/mol) [20] > Pt-Al<sub>2</sub>O<sub>3</sub>-5 (53.7 kJ/mol) [21] > 0.94Pt-1.0rGO/ $\alpha$ -MnO<sub>2</sub> (51.3 kJ/mol). Obviously, our 0.94Pt-1.0rGO/ $\alpha$ -MnO<sub>2</sub> catalyst possessed the lowest  $E_a$  value for benzene oxidation, i.e., this catalyst performed the best among the above catalysts.

### 2.1.2. Catalytic Stability and Effects of GHSV and Benzene Concentration on Catalytic Activity

Catalytic stability is an important feature for evaluating catalytic performance of a sample. Under the different reaction conditions, catalytic activity of the 0.94Pt-1.0rGO/ $\alpha$ -MnO<sub>2</sub> sample fluctuated slightly within 60 h of reaction, but no downward trend was observed (Figure 1C), which proves that catalytic stability of 0.94Pt-1.0rGO/ $\alpha$ -MnO<sub>2</sub> was excellent. Figure 1D shows the effect of GHSV on catalytic activity of 0.94Pt-1.0rGO/ $\alpha$ -MnO<sub>2</sub>. It can be seen that catalytic activity decreased with the rise in GHSV, which might result from the shortening of the contact time between benzene molecules and the catalyst. However, when the GHSV was as high as 240,000 mL/(g h), benzene conversion over 0.94Pt-1.0rGO/ $\alpha$ -MnO<sub>2</sub> at 215 °C still reached 90%. Figure S5 shows the effect of benzene concentration on catalytic activity of 0.94Pt-1.0rGO/ $\alpha$ -MnO<sub>2</sub>. With the increase in benzene concentration, the activity showed a downward trend, but a benzene conversion of 90% was maintained at 205 °C in the case of a high concentration of 4000 ppm benzene, indicating that benzene concentration did not significantly influence the catalytic activity of 0.94Pt-1.0rGO/ $\alpha$ -MnO<sub>2</sub>.

## 2.2. Catalyst Characterization

### 2.2.1. Structure and Morphology

Figure 2 shows XRD patterns of the samples. Diffraction peaks were observed at  $2\theta = 12.9^\circ, 28.9^\circ, 37.7^\circ, 49.9^\circ, 60.3^\circ, \text{ and } 69.7^\circ$ , which corresponded to the (110), (200), (310), (211), (411), (521), and (541) crystal planes, respectively [22]. Obviously, the diffraction peak positions of  $x$ Pt- $y$ rGO/ $\alpha$ -MnO<sub>2</sub> were in good agreement with those of the standard  $\alpha$ -MnO<sub>2</sub> sample (JCPTS PDF# 44-0141), indicating that the crystal structure of  $\alpha$ -MnO<sub>2</sub> remains unchanged after loading of Pt and rGO. The absence of characteristic peaks due to the Pt and rGO phases in the XRD spectra of all of the samples might be due to the fact that Pt and monolayer rGO are uniformly loaded on the surface of  $\alpha$ -MnO<sub>2</sub> nanorods. According to the Scherrer equation, particle sizes of the samples can be calculated, and the results are listed in Table S2. It can be seen that after loading of Pt and/or rGO, peak intensity of  $\alpha$ -MnO<sub>2</sub> became weaker, diffraction peaks were broadened, and the particle size of each sample decreased, which indicates that the loading of Pt and rGO results in a decrease in crystallinity of the sample.

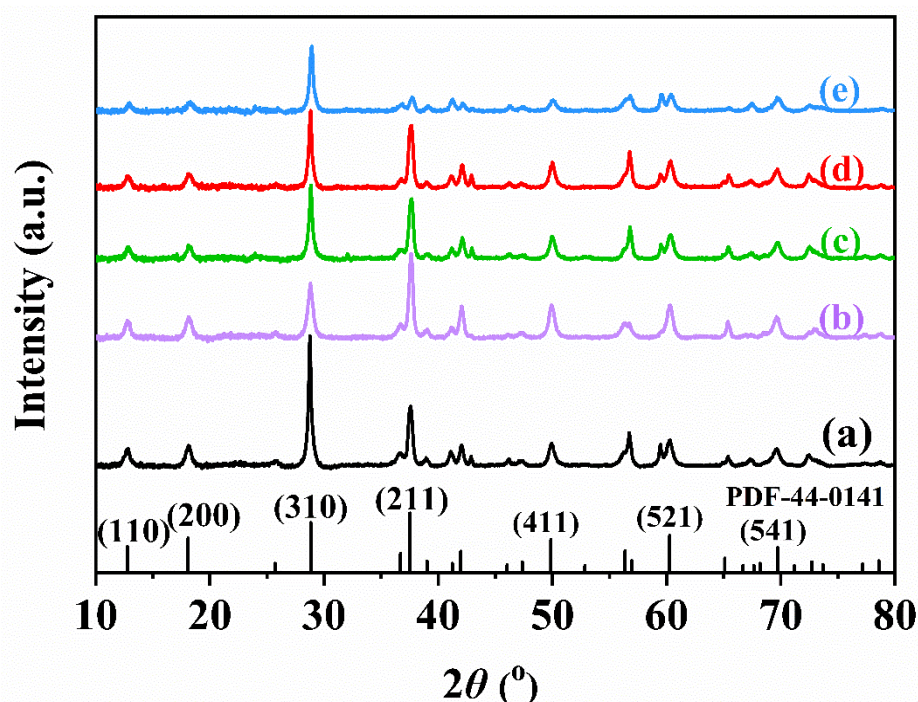


**Figure 2.** XRD patterns of (a)  $\alpha$ -MnO<sub>2</sub>, (b) 0.93Pt/ $\alpha$ -MnO<sub>2</sub>, (c) 0.91Pt-0.5rGO/ $\alpha$ -MnO<sub>2</sub>, (d) 0.94Pt-1.0rGO/ $\alpha$ -MnO<sub>2</sub>, and (e) 0.92Pt-2.0rGO/ $\alpha$ -MnO<sub>2</sub>.

Figure S1 shows FTIR spectra of the samples. The absorption bands around 710 and 595 cm<sup>-1</sup> were attributed to the Mn–O and/or Mn = O stretching vibration of the MnO<sub>6</sub> octahedron in  $\alpha$ -MnO<sub>2</sub>. The positions of the polymorphic vibration bands of all of the samples were almost the same, but intensity of the vibration bands was different, which indicates that all of the samples have similar structures. This outcome was in consistency with the XRD result.

Figure S2 shows the N<sub>2</sub> adsorption–desorption isotherms and pore-size distribution curves of the samples. The N<sub>2</sub> sorption isotherm of each sample (Figure S2A) was type IV with a H<sub>3</sub>-type hysteresis loop at a high relative pressure ( $p/p_0 = 0.5–1.0$ ), indicating that the presence of mesopores was caused by the layered aggregation of the nanorod-shaped  $\alpha$ -MnO<sub>2</sub> particles [23]. The corresponding pore-size distribution (8.1–9.0 nm) was obtained by performing BJH calculations on the adsorption data (Figure S2B), further confirming that the samples are of a mesoporous structure. The textural properties are summarized in Table 2. The surface area (37.9–40.7 m<sup>2</sup>/g) and pore volume (0.071–0.081 cm<sup>3</sup>/g) of each  $x$ Pt- $y$ rGO/ $\alpha$ -MnO<sub>2</sub> sample were higher than those of the rGO-free 0.93Pt/ $\alpha$ -MnO<sub>2</sub> sample (37.1 m<sup>2</sup>/g and 0.060 cm<sup>3</sup>/g), respectively. The results indicate that the loading of rGO gives rise to an increase in surface area and pore volume of the sample, which was beneficial for the diffusion of benzene molecules and thus improved the catalytic activity.

**Table 2.** Surface areas, pore volumes, average pore diameter, and crystallite sizes ( $D$ ) of the samples.

Sample	Surface Area (m <sup>2</sup> /g)	Pore Volume (cm <sup>3</sup> /g)	Average Pore Diameter (nm)	$D^a$ (nm)
$\alpha$ -MnO <sub>2</sub>	36.6	0.067	8.9	27.2
0.93Pt/ $\alpha$ -MnO <sub>2</sub>	37.1	0.060	8.3	27.9
0.91Pt-0.5rGO/ $\alpha$ -MnO <sub>2</sub>	37.9	0.071	9.0	28.7
0.94Pt-1.0rGO/ $\alpha$ -MnO <sub>2</sub>	38.7	0.077	8.5	29.1
0.92Pt-2.0rGO/ $\alpha$ -MnO <sub>2</sub>	40.7	0.087	8.1	33.9

<sup>a</sup> Data determined based on the XRD results according to the Scherrer equation using the FWHM of the (110), (200), (310), and (211) lines of  $\alpha$ -MnO<sub>2</sub>.

The morphology of each sample was observed by the SEM technique to compare the morphological changes of  $\alpha$ -MnO<sub>2</sub> after loading of Pt and/or rGO. As shown in Figure 3, each sample showed a nanorod-like structure. Compared with the  $\alpha$ -MnO<sub>2</sub> sample, the morphology of the rGO-free 0.93Pt/ $\alpha$ -MnO<sub>2</sub> or  $x$ Pt- $y$ rGO/ $\alpha$ -MnO<sub>2</sub> sample did not change significantly. Figure 4 shows HRTEM images of the rGO-free 0.93Pt/ $\alpha$ -MnO<sub>2</sub> and 0.94Pt-1.0rGO/ $\alpha$ -MnO<sub>2</sub> samples. The high-resolution lattice spacings could be clearly observed on the nanorods. The Pt particles were highly dispersed on the surface of the  $\alpha$ -MnO<sub>2</sub> nanorods. Pt particle sizes and their distributions of the samples are shown in Table S2 and Figure S3, respectively. The results show that the average Pt particle sizes of rGO-free 0.93Pt/ $\alpha$ -MnO<sub>2</sub>, 0.91Pt-0.5rGO/ $\alpha$ -MnO<sub>2</sub>, 0.94Pt-1.0rGO/ $\alpha$ -MnO<sub>2</sub>, and 0.92Pt-2.0rGO/ $\alpha$ -MnO<sub>2</sub> were  $3.2 \pm 0.5$ ,  $2.8 \pm 0.6$ ,  $2.7 \pm 0.9$ , and  $2.9 \pm 0.9$  nm, respectively. The average Pt particle sizes in the  $x$ Pt- $y$ rGO/ $\alpha$ -MnO<sub>2</sub> samples were smaller than that in the rGO-free 0.93Pt/ $\alpha$ -MnO<sub>2</sub> sample. The lattice spacings in TEM images (Figure 4a–c) of rGO-free 0.93Pt/ $\alpha$ -MnO<sub>2</sub> were measured to be 0.31 and 0.25 nm, which were assigned to the (310) and (211) crystal planes of the standard  $\alpha$ -MnO<sub>2</sub> sample, respectively. The measured lattice spacings in TEM images of the 0.94Pt-1.0rGO/ $\alpha$ -MnO<sub>2</sub> sample (Figure 4d–f) were 0.31 and 0.47 nm, which were ascribed to the (310) and (200) crystal planes of the standard  $\alpha$ -MnO<sub>2</sub> sample, respectively. The results were consistent with the XRD results. In addition, no rGO morphologies were clearly observed, which might be due to its low loading or its uniformly dispersed state on the sample surface. To further investigate the distribution of Pt nanoparticles on the surface of  $\alpha$ -MnO<sub>2</sub> nanorods, we recorded elemental mappings of the 0.94Pt-1.0rGO/ $\alpha$ -MnO<sub>2</sub> sample (Figure 4g–i). It can be seen from the elemental mappings that the Pt element was evenly distributed on the surface of the 0.94Pt-1.0rGO/ $\alpha$ -MnO<sub>2</sub> sample.

### 2.2.2. Surface Property

The surface elemental composition and chemical state of each sample were characterized by X-ray photoelectron spectroscopy (XPS), and their XPS spectra and quantified analysis results are shown in Figure 5 and Table 3, respectively. The XPS spectra demonstrate the presence of Mn, O, and Pt elements in the 0.94Pt-1.0rGO/ $\alpha$ -MnO<sub>2</sub> sample, which corresponds with the results of elemental mapping analysis (Figure 4). As can be seen from Figure 5A, the components at binding energy (BE) = 640.3, 641.5, and 642.8 eV were attributed to the surface Mn<sup>2+</sup>, Mn<sup>3+</sup>, and Mn<sup>4+</sup> species [24], respectively. Generally speaking, the presence of Mn<sup>2+</sup> and Mn<sup>3+</sup> species is beneficial for the generation of oxygen vacancies on the catalyst surface, thus improving the catalytic activity. The Mn<sup>3+</sup>/Mn<sup>4+</sup> molar ratio decreased in an order of 0.94Pt-1.0rGO/ $\alpha$ -MnO<sub>2</sub> (0.60) > 0.92Pt-2.0rGO/ $\alpha$ -MnO<sub>2</sub> (0.58) > 0.91Pt-0.5rGO/ $\alpha$ -MnO<sub>2</sub> (0.55) > 0.93Pt/ $\alpha$ -MnO<sub>2</sub> (0.50) >  $\alpha$ -MnO<sub>2</sub> (0.48). The Mn<sup>3+</sup>/Mn<sup>4+</sup> molar ratio increased significantly after Pt loading, a result due to the SMSI between Pt and  $\alpha$ -MnO<sub>2</sub> with electron transfer from Pt to  $\alpha$ -MnO<sub>2</sub> (Pt<sup>0</sup> + Mn<sup>4+</sup> → Pt<sup>2+</sup> + Mn<sup>3+</sup>). Furthermore, the molar ratio of Mn<sup>3+</sup>/Mn<sup>4+</sup> was further increased with the loading of rGO, which was attributed to the ability of rGO to transfer electrons, thus promoting the SMSI between Pt and  $\alpha$ -MnO<sub>2</sub>. The oxygens in the loaded rGO formed an effective electron transfer channel between Pt and  $\alpha$ -MnO<sub>2</sub>, hence promoting the catalytic oxidation of benzene [25]. Among all of the samples, 0.94Pt-1.0rGO/ $\alpha$ -MnO<sub>2</sub> shows the highest amount of the Mn<sup>3+</sup> species, which favors the generation of the largest oxygen vacancies and thus are beneficial for the enhancement in catalytic activity.

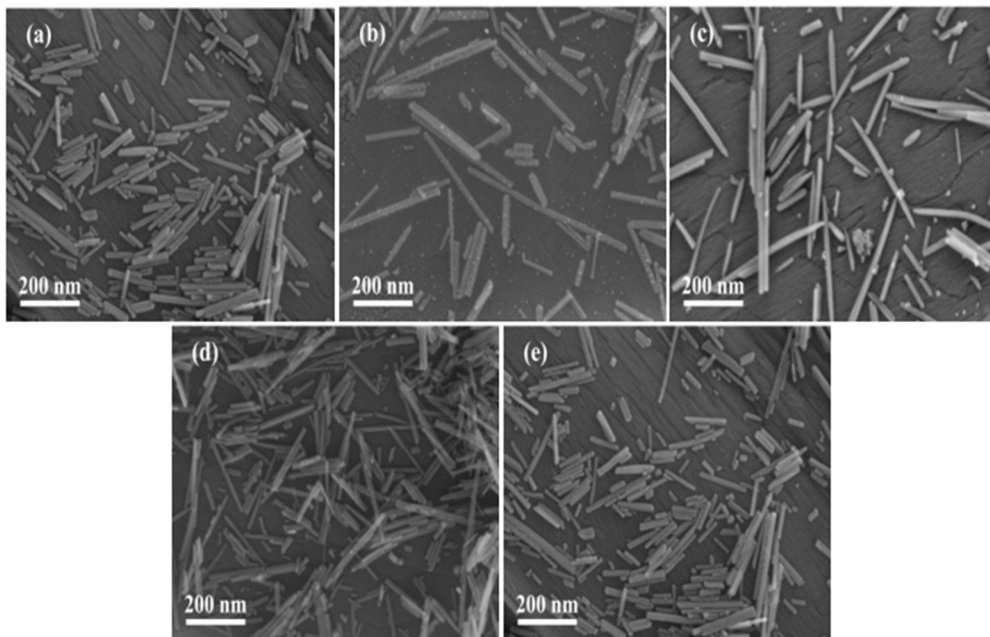


**Figure 3.** SEM images of (a)  $\alpha$ -MnO<sub>2</sub>, (b) 0.93Pt/ $\alpha$ -MnO<sub>2</sub>, (c) 0.91Pt-0.5rGO/ $\alpha$ -MnO<sub>2</sub>, (d) 0.94Pt-1.0rGO/ $\alpha$ -MnO<sub>2</sub>, and (e) 0.92Pt-2.0rGO/ $\alpha$ -MnO<sub>2</sub>.

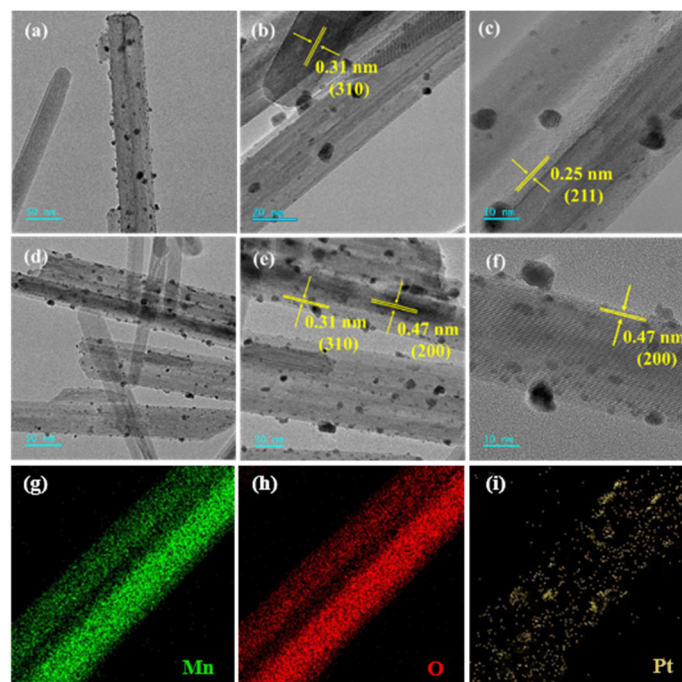


**Figure 4.** (a–f) TEM images of (a–c) 0.93Pt/ $\alpha$ -MnO<sub>2</sub> and (d–f) 0.94Pt-1.0rGO/ $\alpha$ -MnO<sub>2</sub>, and (g–i) elemental mappings of 0.94Pt-1.0rGO/ $\alpha$ -MnO<sub>2</sub>.

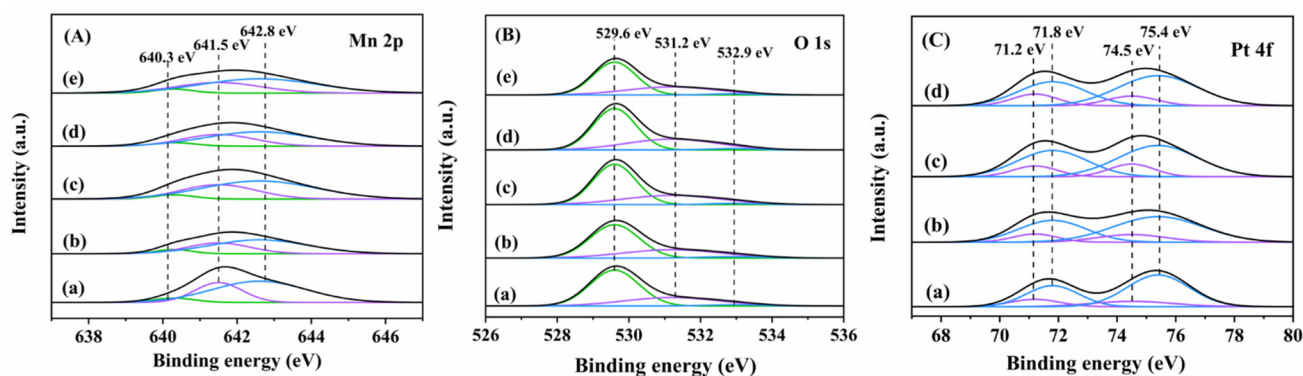


**Figure 5.** (A) Mn 2p, (B) O 1s, and (C) Pt 4f XPS spectra of (a)  $\alpha$ -MnO<sub>2</sub>, (b) 0.93Pt/ $\alpha$ -MnO<sub>2</sub>, (c) 0.91Pt-0.5rGO/ $\alpha$ -MnO<sub>2</sub>, (d) 0.94Pt-1.0rGO/ $\alpha$ -MnO<sub>2</sub>, and (e) 0.92Pt-2.0rGO/ $\alpha$ -MnO<sub>2</sub>.

**Table 3.** Surface element compositions and H<sub>2</sub> consumption of the samples.

Sample	Surface Element Composition (Molar Ratio)			H <sub>2</sub> Consumption (mmol/g)			
	Mn <sup>3+</sup> /Mn <sup>4+</sup>	Pt <sup>2+</sup> /Pt <sup>0</sup>	O <sub>ads</sub> /O <sub>latt</sub>	$\alpha$	$\beta$	$\gamma$	Total
$\alpha$ -MnO <sub>2</sub>	0.48	–	0.45	16.3	18.5	6.7	41.5
0.93Pt/ $\alpha$ -MnO <sub>2</sub>	0.50	0.50	0.50	20.9	14.3	8.6	43.8
0.91Pt-0.5rGO/ $\alpha$ -MnO <sub>2</sub>	0.55	0.57	0.53	21.1	13.1	9.9	44.1
0.94Pt-1.0rGO/ $\alpha$ -MnO <sub>2</sub>	0.60	0.61	0.57	23.3	14.2	9.8	47.3
0.92Pt-2.0rGO/ $\alpha$ -MnO <sub>2</sub>	0.58	0.59	0.55	29.8	12.8	10.5	46.1

As shown in Figure 5B, O 1s XPS spectra of the samples were split into three components at BE = 529.6 eV, 531.2 eV, and 532.9 eV, which were due to the surface lattice oxygen (O<sub>latt</sub>), adsorbed oxygen (O<sub>ads</sub>), and hydroxyl or adsorbed water [26], respectively. As shown in Table 3, the O<sub>ads</sub>/O<sub>latt</sub> molar ratio decreased in the sequence of 0.94Pt-1.0rGO/ $\alpha$ -MnO<sub>2</sub> (0.57) > 0.92Pt-2.0rGO/ $\alpha$ -MnO<sub>2</sub> (0.55) > 0.91Pt-0.5rGO/ $\alpha$ -MnO<sub>2</sub> (0.53) > 0.93Pt/ $\alpha$ -MnO<sub>2</sub> (0.50) >  $\alpha$ -MnO<sub>2</sub> (0.45). The O<sub>ads</sub>/O<sub>latt</sub> molar ratio increased obviously after Pt loading. Moreover, the molar ratio of O<sub>ads</sub>/O<sub>latt</sub> further increased after loading of rGO, which exhibits the same changing trend as the Mn<sup>3+</sup>/Mn<sup>4+</sup> molar ratio. Among all of the samples, 0.94Pt-1.0rGO/ $\alpha$ -MnO<sub>2</sub> possessed the highest O<sub>ads</sub>/O<sub>latt</sub> molar ratio, therefore the highest oxygen mobility and oxidation capacity. The benzene catalytic oxidation proceeds by electron transfer between the metal oxide, reactants, and formed intermediate species, and the oxygen mobility and oxidation capacity of a catalyst played a major role in the catalytic oxidation of benzene [27]. It indicates that the loading of Pt and rGO can enhance the catalytic oxidation activity by increasing the oxygen vacancies of  $\alpha$ -MnO<sub>2</sub>.

As shown in Figure 5C, Pt 4f could be divided into two Pt 4f<sub>7/2</sub> and Pt 4f<sub>5/2</sub> sub-peaks with BE = 71.2 and BE = 74.5 eV (the surface Pt<sup>0</sup> species) and BE = 71.8 and BE = 75.4 eV (the surface Pt<sup>2+</sup> species). Generally speaking, a higher Pt<sup>2+</sup> content means more Pt–O bonds and higher dispersion of Pt in the catalyst. The Pt<sup>2+</sup>/Pt<sup>0</sup> molar ratio decreased in the order of 0.94Pt-1.0rGO/ $\alpha$ -MnO<sub>2</sub> (0.61) > 0.92Pt-2.0rGO/ $\alpha$ -MnO<sub>2</sub> (0.59) > 0.91Pt-0.5rGO/ $\alpha$ -MnO<sub>2</sub> (0.57) > 0.93Pt/ $\alpha$ -MnO<sub>2</sub> (0.50), which was consistent with the order in Mn<sup>3+</sup>/Mn<sup>4+</sup> or O<sub>ads</sub>/O<sub>latt</sub> molar ratio, as well as with the order in catalytic activity. The molar ratios (0.57–0.61) of Pt<sup>2+</sup>/Pt<sup>0</sup> on the *x*Pt-rGO/ $\alpha$ -MnO<sub>2</sub> samples were higher than that (0.50) of the rGO-free 0.93Pt/ $\alpha$ -MnO<sub>2</sub> sample, indicating that the introduction of rGO into Pt/ $\alpha$ -MnO<sub>2</sub> strengthened the SMSI between Pt and  $\alpha$ -MnO<sub>2</sub>. Among all of the samples, 0.94Pt-1.0rGO/ $\alpha$ -MnO<sub>2</sub> showed the highest molar ratios of Pt<sup>2+</sup>/Pt<sup>0</sup>, Mn<sup>3+</sup>/Mn<sup>4+</sup>, and O<sub>ads</sub>/O<sub>latt</sub>, indicating that this sample possessed the strongest SMSI between Pt and  $\alpha$ -MnO<sub>2</sub>.

### 2.2.3. Low-Temperature Reducibility and Adsorption Ability

To investigate the reducibility of the samples, H<sub>2</sub>-TPR experiments were performed, and their H<sub>2</sub>-TPR profiles are shown in Figure 6. The H<sub>2</sub>-TPR curve of each sample could

be decomposed into three peaks, defined as  $\alpha$ ,  $\beta$ , and  $\gamma$  peaks. For the  $\alpha$ -MnO<sub>2</sub> sample, the  $\alpha$  peak (315 °C),  $\beta$  peak (371 °C), and  $\gamma$  peak (467 °C) were attributed to the successive reduction of  $\alpha$ -MnO<sub>2</sub> (i.e., MnO<sub>2</sub> → Mn<sub>2</sub>O<sub>3</sub> → Mn<sub>3</sub>O<sub>4</sub> → MnO) [28]. After loading of Pt, all of the reduction peaks were significantly moved to lower temperatures (for example, the temperature of the  $\alpha$  peak was significantly decreased from 315 to 192–196 °C), which indicates that the reducibility of the sample was much improved. Moreover, compared with  $\alpha$ -MnO<sub>2</sub>, the new low-temperature peak of the Pt-loaded sample appeared around 120 °C, corresponding to the reduction of the oxidized Pt species [29]. The temperatures of the reduction peaks for the rGO-loaded and rGO-free samples were almost the same, but the H<sub>2</sub> consumption of the rGO-loaded sample was significantly larger than that of the rGO-free sample (Table 3). The above results show that the loading of Pt and rGO on  $\alpha$ -MnO<sub>2</sub> can greatly increase the reactivity of lattice oxygen, thus improving redox ability of the sample. Among all of the samples, 0.94Pt-1.0rGO/ $\alpha$ -MnO<sub>2</sub> exhibited the lowest reduction temperature (192 °C) and the highest hydrogen consumption (47.3 mmol/g), thus exhibiting the best catalytic oxidation performance. Hence, we conclude that the SMSI between Pt or rGO and  $\alpha$ -MnO<sub>2</sub> contributed to the enhancement in catalytic performance of 0.94Pt-1.0rGO/ $\alpha$ -MnO<sub>2</sub>.

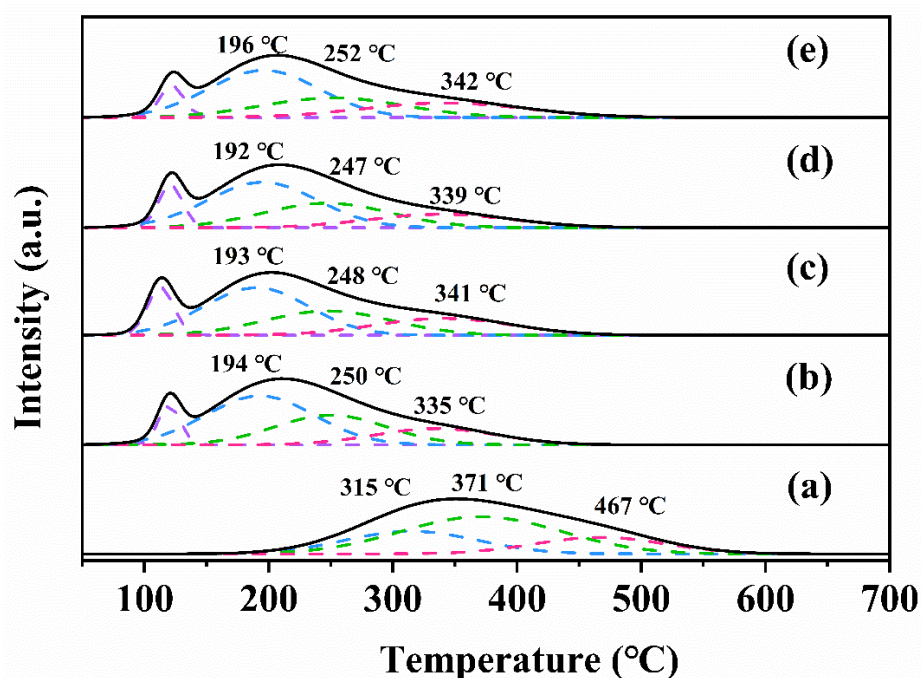


**Figure 6.** H<sub>2</sub>-TPR profiles of (a)  $\alpha$ -MnO<sub>2</sub>, (b) 0.93Pt/ $\alpha$ -MnO<sub>2</sub>, (c) 0.91Pt-0.5rGO/ $\alpha$ -MnO<sub>2</sub>, (d) 0.94Pt-1.0rGO/ $\alpha$ -MnO<sub>2</sub>, and (e) 0.92Pt-2.0rGO/ $\alpha$ -MnO<sub>2</sub>.

Figure S4 shows O<sub>2</sub>-TPD profiles of the samples. The peaks in each O<sub>2</sub>-TPD curve could be divided into three parts: The low-temperature peaks at 150–200 °C were attributed to desorption of the surface chemisorbed oxygen species, the medium-temperature peaks at 550–650 °C were ascribed to desorption of the lattice oxygen (O<sub>ads</sub>) species close to the sample surface, and the high-temperature peaks at 750–850 °C were assigned to desorption of the bulk lattice oxygen (O<sub>latt</sub>) species [30]. Areas and intensity of the medium- and high-temperature peaks of the 0.93Pt/ $\alpha$ -MnO<sub>2</sub> and  $x$ Pt- $y$ rGO/ $\alpha$ -MnO<sub>2</sub> samples were larger or higher than those of the  $\alpha$ -MnO<sub>2</sub> sample, indicating that the loading of Pt and rGO enhanced the amount of surface and bulk lattice oxygen species, thus improving redox ability of the catalyst. The  $x$ Pt- $y$ rGO/ $\alpha$ -MnO<sub>2</sub> sample showed a stronger intensity and a larger area of the medium-temperature peak than the rGO-free 0.93Pt/ $\alpha$ -MnO<sub>2</sub> sample, demonstrating that the loading of rGO strengthened the SMSI between Pt and  $\alpha$ -MnO<sub>2</sub>, which enhanced the desorption amount of lattice oxygen [31]. This result was consistent

with the above XPS and H<sub>2</sub>-TPR results. Among all of the samples, 0.94Pt-1.0rGO/ $\alpha$ -MnO<sub>2</sub> exhibited the lowest desorption temperature, indicating the easiest release of lattice oxygen and the best oxygen mobility, which was beneficial for the enhancement in catalytic activity of the sample.

### 2.3. Effects of Water Vapor and SO<sub>2</sub> on Catalytic Activity

Since the actual industrial VOCs emissions usually contain H<sub>2</sub>O, SO<sub>2</sub>, and other components, it is necessary to study the influence of these gases on catalytic performance of the typical sample. Figure 7A shows catalytic activity of the 0.94Pt-1.0rGO/ $\alpha$ -MnO<sub>2</sub> sample for benzene oxidation at 170 °C and GHSV = 60,000 mL/(g h) in the presence of 1.0, 3.0, and 5.0 vol% water vapor, respectively. When 1.0 vol% water vapor was introduced to the reaction system, catalytic activities were hardly changed, indicating that 1.0 vol% water vapor did not affect catalytic benzene oxidation over this sample. After 3.0 vol% water vapor was added, catalytic activity was slightly decreased. Moreover, when the water supply was cut off, catalytic activity was gradually returned to the original level. After 5.0 vol% water vapor was introduced, however, catalytic activity was significantly decreased, and benzene conversion was dropped to 75%. After cutting off water vapor, catalytic activity was gradually increased, but not restored to the original level. These results indicate that partial deactivation of the 0.94Pt-1.0rGO/ $\alpha$ -MnO<sub>2</sub> sample caused by the introduction of water vapor is reversible. There were the competitive adsorption of water vapor and reactant (benzene and oxygen) molecules on the sample surface [32]. When the humidity in the feed stream decreased, such a deactivation could be restored to a large extent. However, after frequent switching of the humidity conditions, benzene conversion over 0.94Pt-1.0rGO/ $\alpha$ -MnO<sub>2</sub> was gradually decreased with the extension of reaction time, indicating that simply cutting off the water vapor supply could not fully restore catalytic activity of the sample.

To study the effect of SO<sub>2</sub> on catalytic activity of 0.94Pt-1.0rGO/ $\alpha$ -MnO<sub>2</sub>, 25, 50, or 75 ppm SO<sub>2</sub> was added to the benzene oxidation system, and their activity data are shown in Figure 7B. The introduction of SO<sub>2</sub> exerted a negative impact on catalytic activity of 0.94Pt-1.0rGO/ $\alpha$ -MnO<sub>2</sub>. Compared with the SO<sub>2</sub>-free case, the  $T_{90\%}$  value increased by 10, 21, and 36 °C after 25, 50, and 75 ppm SO<sub>2</sub> were introduced, respectively. Therefore, the addition of different SO<sub>2</sub> concentrations decreased the catalytic activity of 0.94Pt-1.0rGO/ $\alpha$ -MnO<sub>2</sub> to various extents. This result might result from the fact that some of the active sites in 0.94Pt-1.0rGO/ $\alpha$ -MnO<sub>2</sub> were covered by the generated sulfate species, which hindered the adsorption and catalytic reaction of benzene and oxygen on the sample surface, thus decreasing catalytic activity of the sample [33].

To examine the influence of SO<sub>2</sub> introduction on catalytic activity of different samples, Figure 7C–E shows the sulfur dioxide resistance experiments of  $\alpha$ -MnO<sub>2</sub>, 0.93Pt/ $\alpha$ -MnO<sub>2</sub>, and 0.94Pt-1.0rGO/ $\alpha$ -MnO<sub>2</sub>. After introducing 50 ppm SO<sub>2</sub> to the reaction system (50 ppm is a relatively moderate concentration, so it was adopted to investigate the effect of SO<sub>2</sub> on catalytic activity of the samples), the reaction time required for benzene conversion dropped to 70% over  $\alpha$ -MnO<sub>2</sub>, 0.93Pt/ $\alpha$ -MnO<sub>2</sub>, 0.94Pt-1.0rGO/ $\alpha$ -MnO<sub>2</sub> was 8, 14, and 27 h, respectively. Therefore, sulfur dioxide resistance decreased in the order of 0.94Pt-1.0rGO/ $\alpha$ -MnO<sub>2</sub> > 0.93Pt/ $\alpha$ -MnO<sub>2</sub> >  $\alpha$ -MnO<sub>2</sub>. This result was associated with the loading of Pt and rGO on the surface of  $\alpha$ -MnO<sub>2</sub> nanorods. It was found that the loading of Pt and rGO hindered the chemisorption of SO<sub>2</sub> and prevented the active site of the catalyst from being poisoned by SO<sub>2</sub>, thus enhancing sulfur dioxide resistance of the catalyst.

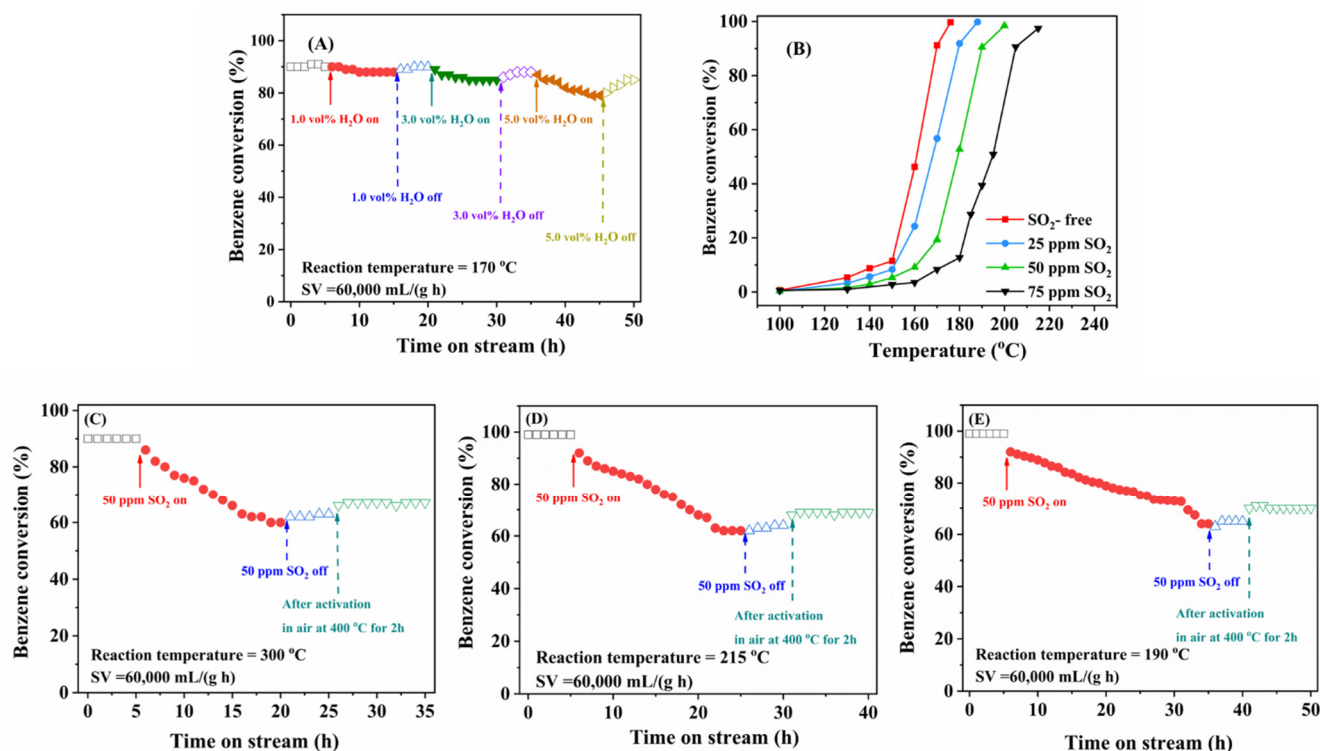


**Figure 7.** (A) Effect of water vapor on the conversion of benzene over the 0.94Pt-1.0rGO/ $\alpha$ -MnO<sub>2</sub> sample at 170 °C and SV = 60,000 mL/(g h), (B) effect of SO<sub>2</sub> on catalytic activity of the 0.94Pt-1.0rGO/ $\alpha$ -MnO<sub>2</sub> sample for benzene oxidation at SV = 60,000 mL/(g h), and effect of 75 ppm SO<sub>2</sub> on benzene conversion over (C)  $\alpha$ -MnO<sub>2</sub>, (D) 0.93Pt/ $\alpha$ -MnO<sub>2</sub>, and (E) 0.94Pt-1.0rGO/ $\alpha$ -MnO<sub>2</sub> at benzene concentration = 1000 ppm and different temperatures.

#### 2.4. Physicochemical Characterization Analysis of the Catalyst after SO<sub>2</sub> Poisoning

To further investigate the reason for the decrease in activity of the SO<sub>2</sub>-poisoning samples, 50 ppm SO<sub>2</sub> was passed through the fresh 0.94Pt-1.0rGO/ $\alpha$ -MnO<sub>2</sub> sample for 30 h (the obtained sulfur dioxide-poisoned sample was denoted as 0.94Pt-1.0rGO/ $\alpha$ -MnO<sub>2</sub>-S). XPS, XRD, FT-IR, H<sub>2</sub>-TPR, and TG characterization experiments of the fresh and 0.94Pt-1.0rGO/ $\alpha$ -MnO<sub>2</sub>-S samples were carried out.

To analyze the changes in surface elements of the samples before and after sulfur dioxide-poisoning, XPS characterization was performed, and the results are shown in Figure 8. Figure 8A shows S 2p spectra of the sulfur dioxide-poisoned sample. S 2p XPS spectrum of each sample was divided by fitting into two components at BE = 168.5 and 169.9 eV, which were attributed to the different surface sulfate species. Figure 8B shows Mn 2p XPS spectra of the fresh and sulfur dioxide-poisoned samples. The Mn<sup>3+</sup>/Mn<sup>4+</sup> molar ratio (0.60) on the fresh sample decreased, as compared with that (0.47) on the sulfur dioxide-poisoned sample. Figure 8C illustrates O 1s XPS spectra of the fresh and the sulfur dioxide-poisoned samples. The O<sub>ads</sub>/O<sub>latt</sub> molar ratio decreased from 0.57 for the fresh sample to 0.46 for the sulfur dioxide-poisoned sample, indicating that SO<sub>2</sub> decreased the amount of the adsorbed oxygen species, which was consistent with the decrease in amount of the surface Mn<sup>3+</sup> species. In addition, Figure 8D shows Pt 4f XPS spectra of the fresh and sulfur dioxide-poisoned samples. The molar ratio of Pt<sup>2+</sup>/Pt<sup>0</sup> decreased slightly after sulfur dioxide-poisoning (from 0.61 for the fresh sample to 0.57 for the sulfur dioxide-poisoned sample). The Pt species was less affected by SO<sub>2</sub> than the Mn species, indicating that Pt possesses better sulfur dioxide resistance. This result suggests that partial deactivation of the sample was mainly due to the deactivation of the  $\alpha$ -MnO<sub>2</sub> support.

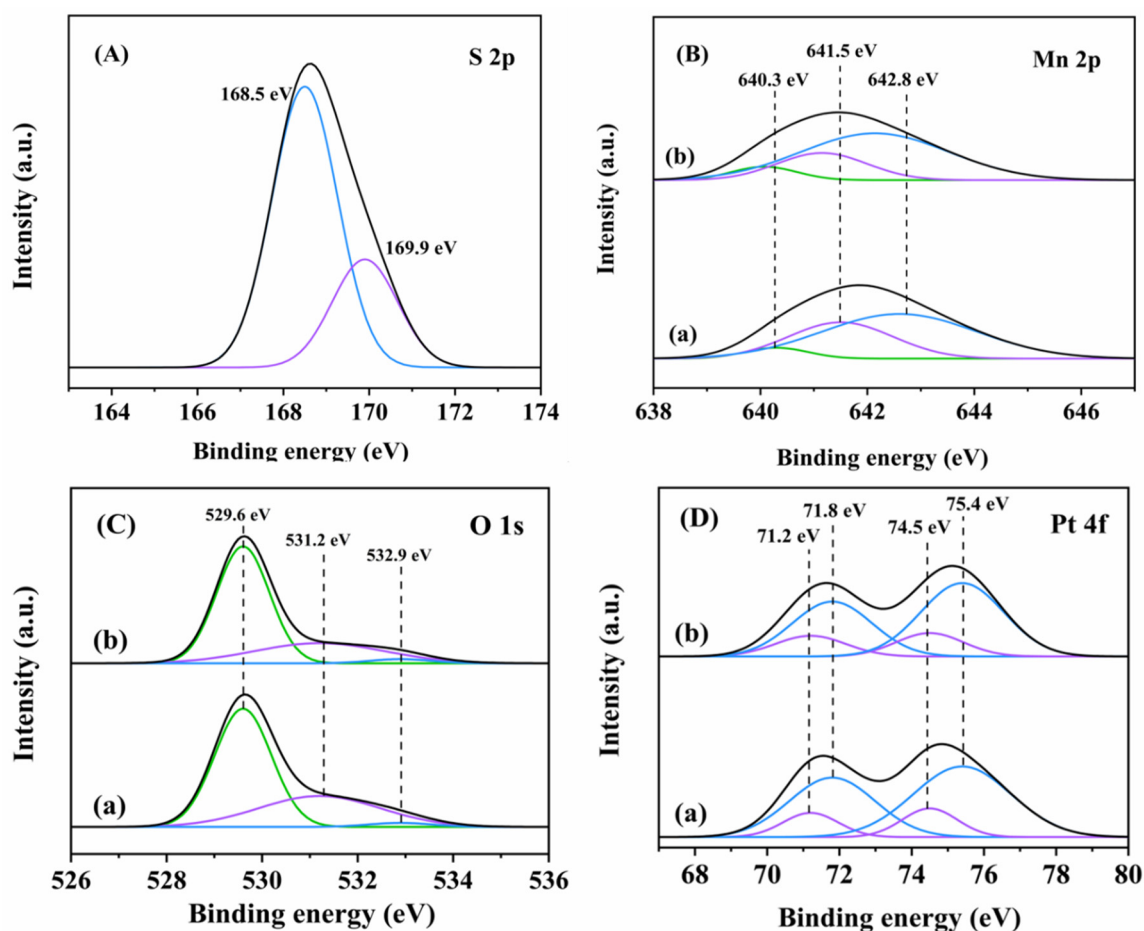
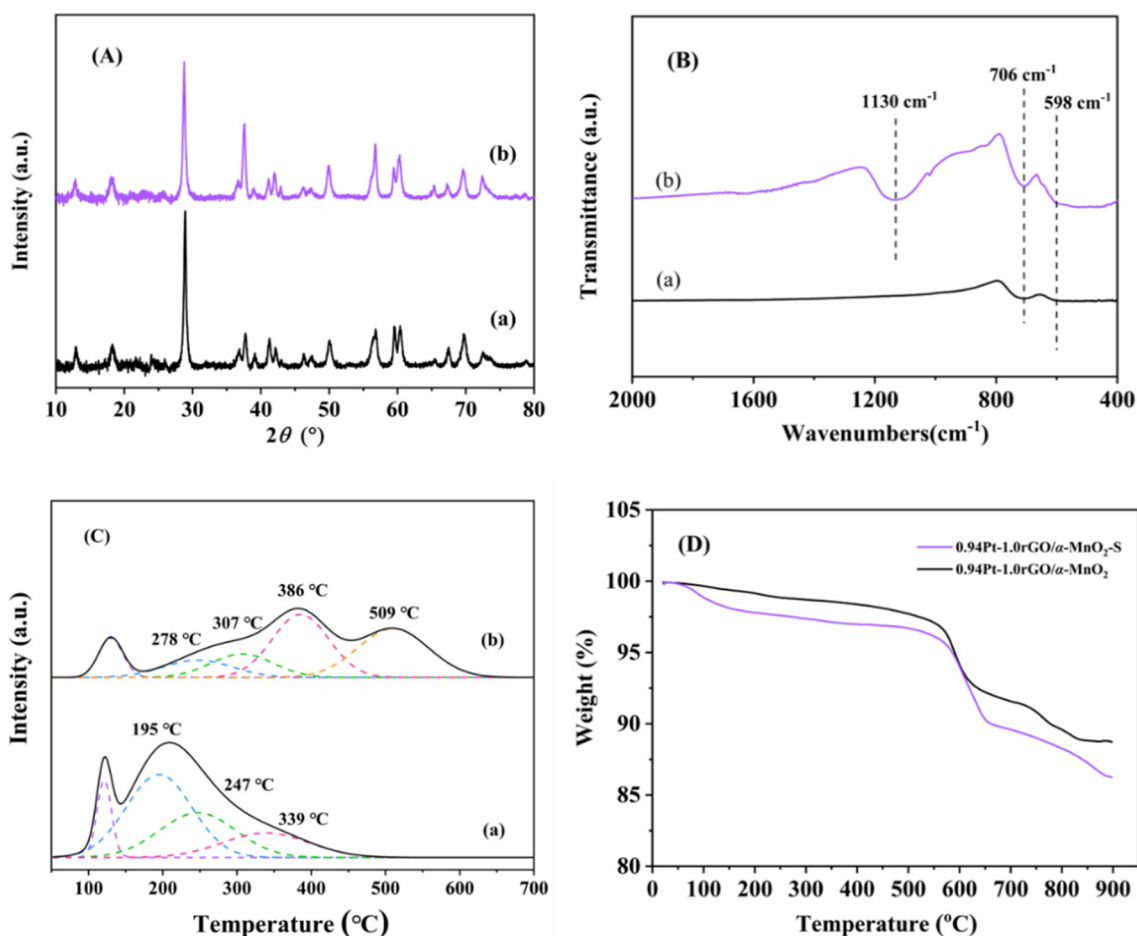


**Figure 8.** (A) S 2p, (B) Mn 2p, (C) O 1s, and (D) Pt 4f XPS spectra of (a) 0.94Pt-1.0rGO/ $\alpha$ -MnO<sub>2</sub> and (b) 0.94Pt-1.0rGO/ $\alpha$ -MnO<sub>2</sub>-S.

XRD patterns of the fresh and sulfur dioxide-poisoned samples are shown in Figure 9A. It can be seen from Figure 9A that diffraction peaks of the two samples were consistent with those of the standard  $\alpha$ -MnO<sub>2</sub> sample (JCPDS PDF# 44-0141), indicating that sulfide generation did not affect the crystal structure of  $\alpha$ -MnO<sub>2</sub>. Compared with XRD patterns of the fresh sample, there were no diffraction peaks of sulfide species, such as MnSO<sub>4</sub> and other substances on the sulfur dioxide-poisoned sample, which was due to the fact that sulfate species are mainly present in amorphous form and therefore not detected. Figure 9B shows FT-IR spectra of the fresh and the sulfur dioxide-poisoned samples. The absorption bands due to the sulfate species were located in the range of 1040–1210 cm<sup>-1</sup>. The sulfur dioxide-poisoned sample exhibited an absorption band at 1130 cm<sup>-1</sup> (functional group sulfation), indicating the formation of sulfate species on the sulfur dioxide-poisoned sample [34].

Figure 9C shows H<sub>2</sub>-TPR spectra of the fresh and sulfur dioxide-poisoned samples. Compared with the fresh sample, intensity of the reduction peak in the low-temperature region of the sulfur dioxide-poisoned sample was significantly weakened, and the reduction peak tended to shift to the high-temperature region, indicating that reducibility of the sulfur dioxide-poisoned sample was weakened, especially the low-temperature reducibility. At the same time, a strong reduction peak appeared around 509 °C for the sulfur dioxide-poisoning sample, which was attributed to the reduction of the sulfate species, as pointed out by Kijlstra et al. [35]. Combined with other characterization results, we speculate that SO<sub>2</sub> in the mixture reacts with the metal elements in the sample and produced sulfate, which then accumulated over time, deposited on the surface of 0.94Pt-1.0rGO/ $\alpha$ -MnO<sub>2</sub>,

and blocked oxygen vacancies of the sample, thus inhibiting the catalytic reaction and leading to a decrease in catalytic activity [36].



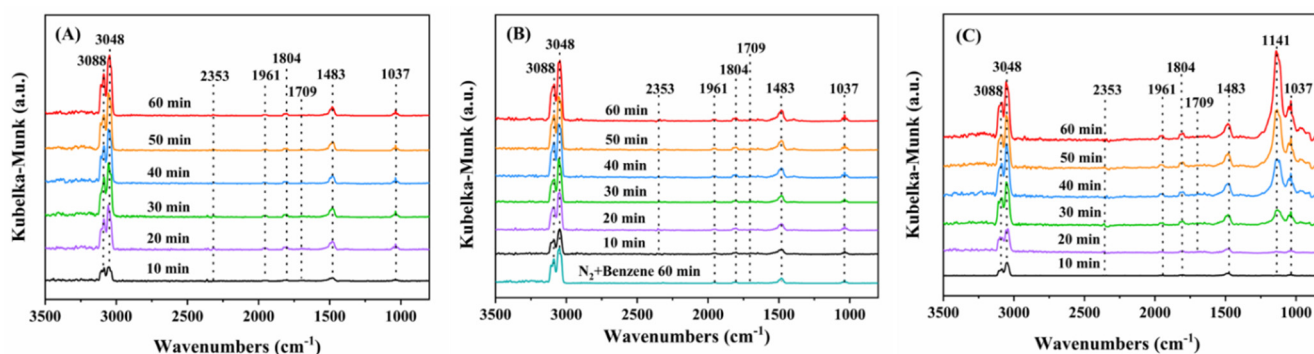
**Figure 9.** (A) XRD patterns, (B) FTIR spectra, (C) H<sub>2</sub>-TPR profiles, and (D) TG profiles of (a) 0.94Pt-1.0rGO/α-MnO<sub>2</sub> and (b) 0.94Pt-1.0rGO/α-MnO<sub>2</sub>-S.

Figure 9D shows thermogravimetric analysis (TG) curves of the fresh and sulfur dioxide-poisoned samples. In the temperature range of 80–200  $^\circ$ C, the weight loss of the fresh or sulfur dioxide-poisoned sample was due to the loss of adsorbed water on the sample surface. The weight loss at 200–550  $^\circ$ C was due to the escape of surface oxygen species and some surface lattice oxygen species on the sample [37]. The weight loss at 550–650  $^\circ$ C was due to the destruction of the rGO structure [38]. Wu et al. [39] pointed out that MnSO<sub>4</sub> was decomposed at 750  $^\circ$ C, so the weight loss of the poisoned sample at 650–850  $^\circ$ C was attributed to the decomposition of MnSO<sub>4</sub>. At the same time, the weight loss of the sulfur dioxide-poisoned sample was bigger than that of the fresh sample, and the weight loss rate was higher. Combined with the H<sub>2</sub>-TPR and TG profiles, we think that during the poisoning process of the sample, a large part of the active Mn component in manganese dioxide is sulfated to form MnSO<sub>4</sub>, which leads to a significant decrease in catalytic activity of the sample.

### 2.5. In Situ DRIFTS Studies

The reaction mechanism of benzene oxidation over 0.94Pt-1.0rGO/α-MnO<sub>2</sub> was investigated by the in situ DRIFTS technique to explore the intermediate species produced during benzene adsorption and oxidation, and their in situ DRIFTS spectra are shown in Figure 10A and B, respectively. Before the experiment, the sample was pretreated in a N<sub>2</sub> flow and cooled to RT after pretreatment at 400  $^\circ$ C for 1 h. Figure 10A shows in situ DRIFTS

spectra of the O<sub>2</sub>-free gas mixture (1000 ppm benzene + N<sub>2</sub> (balance)) adsorption at 160 °C for 10–60 min. As shown in Figure 10A, a series of vibrational bands at 3000–3500 cm<sup>-1</sup> were attributed to the chemisorption of benzene on the Mn<sup>4+</sup> species in MnO<sub>2</sub> [40]. The vibrational bands at 3088 and 3048 cm<sup>-1</sup> were considered to be stretching vibrations of the C–H bonds in the benzene ring [41]. The vibrational bands at 1961 and 1804 cm<sup>-1</sup> were ascribed to the out-of-plane bending mode of C–H bonds [42]. The band at 1709 cm<sup>-1</sup> was thought to be a stretching vibration of C = O bond, presumably producing quinones or ketones [43]. The band at 1483 cm<sup>-1</sup> was owing to be the characteristic signal of the carboxylic acid species, which was the result of the oxidative ring-opening of benzene [44]. The intensity of the band at 1483 cm<sup>-1</sup> increased monotonically with time, indicating the accumulation of organic by-products on the sample surface. The weak vibrational band at 2353 cm<sup>-1</sup> was the characteristic signal of CO<sub>2</sub> [45]. The in situ DRIFTS spectra after the introduction of 20 vol% O<sub>2</sub> in this reaction system are shown in Figure 10B. In comparison with the O<sub>2</sub>-free case, the position of each vibrational band did not change after O<sub>2</sub> addition, but intensity and area of each characteristic band became stronger or larger in the same period. This result indicates that the intermediate species produced after benzene adsorption and oxidation are the same. In the O<sub>2</sub>-free case, the 0.94Pt-1.0rGO/α-MnO<sub>2</sub> sample adsorbed benzene and the O<sub>ads</sub> species on the sample catalyzed the reaction with benzene.



**Figure 10.** In situ DRIFTS spectra of the 0.94Pt-1.0rGO/α-MnO<sub>2</sub> samples in the presence of (A) (1000 ppm benzene + N<sub>2</sub> (balance)), (B) (1000 ppm benzene + 20 vol% O<sub>2</sub> + N<sub>2</sub> (balance)), and (C) (1000 ppm benzene + 50 ppm SO<sub>2</sub> + 20 vol% O<sub>2</sub> + N<sub>2</sub> (balance)) after 10–60 min of reaction at 160 °C.

To further explore the effect of SO<sub>2</sub>, we investigated the intermediates formed during benzene oxidation over the 0.94Pt-1.0rGO/α-MnO<sub>2</sub> sample. Figure 10C shows in situ DRIFTS spectra of the (1000 ppm benzene + 50 ppm SO<sub>2</sub> + 20 vol% O<sub>2</sub> + N<sub>2</sub> (balance)) adsorption at 160 °C for 10–60 min. In comparison with the SO<sub>2</sub>-free case, a strong vibrational band appeared at 1141 cm<sup>-1</sup>, which was considered as the characteristic peak of sulfate [34]. Intensity of the band gradually increased with the introduction of SO<sub>2</sub>, indicating a gradual accumulation of the sulfate species on the sample surface.

After analyzing the in situ DRIFTS spectra and in connection with the previously reported results [46], we propose a possible catalytic benzene oxidation mechanism as follows: First, benzene is oxidized to phenolics by the reactive oxygen species; then, the generated phenolics are converted to benzoquinone; finally, the aromatic ring is destroyed to carboxylic acids, which are further oxidized by the oxygen species to generate CO<sub>2</sub> and H<sub>2</sub>O [47].

According to the literature [48], the surface layer of rGO is evenly distributed with a large specific surface area and an abundant pore structure. Abundant oxygen-containing functional groups exist on the surface of rGO, which favors adsorption of the pollutants. Therefore, the addition of rGO can increase the adsorption sites of benzene. According to the literature [49], as verified by the photocurrent, rGO composite can significantly enhance the intensity of electric current. This result indicates that rGO can enhance the electron

interaction between Ag and  $\text{ZnFe}_2\text{O}_4$  nanoparticles and accelerate the charge migration. Therefore, rGO can act as an electron transfer channel for noble metals or metal oxides, thus facilitating the electron transfer between them. Thus, rGO doping can promote the electronic transfer between Pt and  $\alpha\text{-MnO}_2$  and increase the SMSI between Pt and  $\alpha\text{-MnO}_2$ . As shown in Figure 11, rGO not only provides more sites for benzene adsorption, but also enhances the SMSI between Pt and  $\alpha\text{-MnO}_2$ , thus increasing the content and activation of lattice oxygen on the manganese oxide surface and promoting the deep oxidation of benzene [49]. Therefore, the 0.94Pt-1.0rGO/ $\alpha\text{-MnO}_2$  sample exhibited excellent catalytic performance for benzene oxidation. On the other hand, the loading of Pt and rGO hindered the chemisorption of  $\text{SO}_2$  on the sample and prevented the active sites from being poisoned by  $\text{SO}_2$ , thus enhancing the sulfur dioxide resistance of the sample. However, the overloading of rGO might block and inhibit the active sites of the sample and weaken the SMSI between Pt and  $\alpha\text{-MnO}_2$ , which explained why catalytic activity was decreased when the rGO content increased to 2.0 wt%.

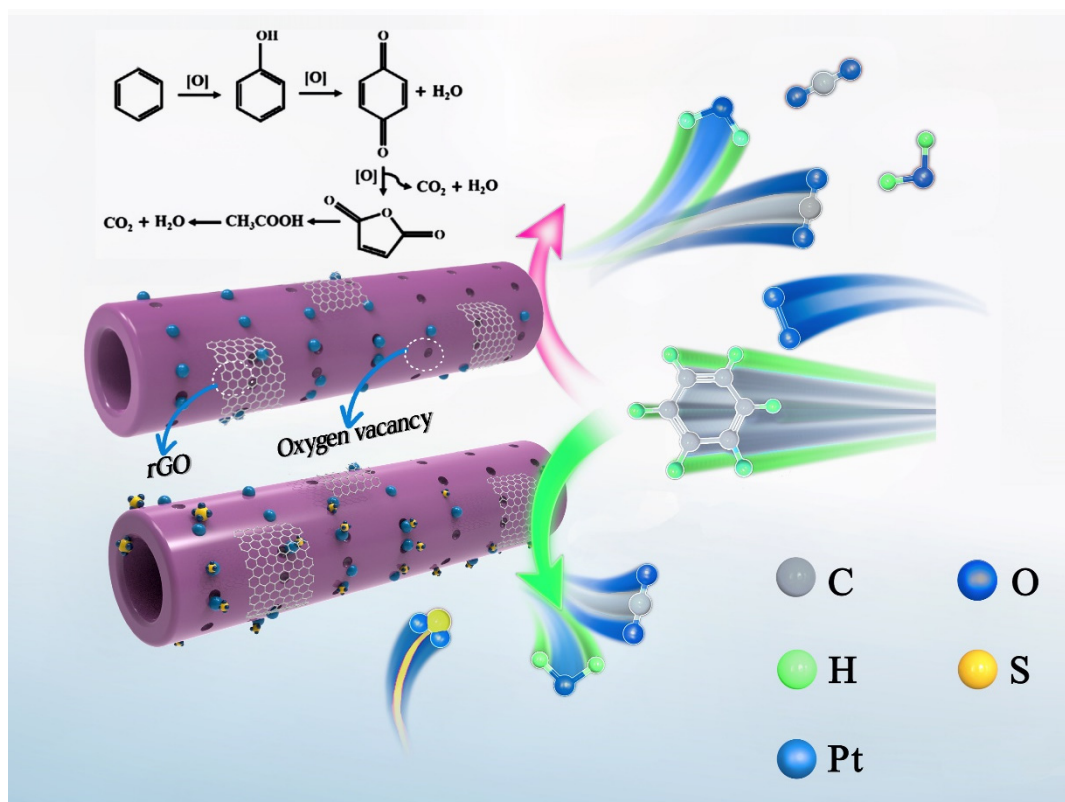


**Figure 11.** Proposed catalytic mechanism of benzene oxidation over 0.94Pt-1.0rGO/ $\alpha\text{-MnO}_2$ .

### 3. Experimental Section

#### 3.1. Preparation of Catalysts

##### 3.1.1. Synthesis of $\alpha\text{-MnO}_2$ Nanorods

The  $\alpha\text{-MnO}_2$  nanorods used in this study were synthesized by the hydrothermal method. The procedure included: dissolving the reactants in deionized water to prepare a mixed aqueous solution, then transferring it to an autoclave, and dissolving and recrystallizing the substances that are insoluble or insoluble at room temperature (RT) under high-pressure and high-temperature conditions by controlling the temperature and hydrothermal time. In a typical synthesis, 0.948 g of  $\text{KMnO}_4$  was added to 90 mL of deionized water, and 1.5 g of  $\text{MnSO}_4 \cdot \text{H}_2\text{O}$  was added to 60 mL of deionized water and continuously stirred for 30 min. Then, the aqueous solution of  $\text{KMnO}_4$  was mixed in the aqueous solution of  $\text{MnSO}_4 \cdot \text{H}_2\text{O}$ . After continuing to stir for 2 h, the mixed aqueous solution was poured into a 200-mL autoclave with a PTFE liner, placed in an oven, and hydrothermally treated

at 165 °C for 24 h. After the reaction kettle was cooled to RT, the reaction kettle was opened to extract the black solid, and the oven temperature was adjusted to 100 °C for drying for 12 h. Finally, the sample was put into a muffle furnace and the heating rate was adjusted to 3 °C/min to calcine the sample from RT to 400 °C and kept at 400 °C for 2 h, thus obtaining the  $\alpha$ -MnO<sub>2</sub> nanorods.

### 3.1.2. Preparation of xPt-yrGO/ $\alpha$ -MnO<sub>2</sub>

The xPt-yrGO/ $\alpha$ -MnO<sub>2</sub> ( $x$  and  $y$  are the mass loadings of Pt and rGO, respectively) catalysts were prepared using the PVA-protecting reduction strategy. Herein, we take the preparation of 1Pt-1rGO/ $\alpha$ -MnO<sub>2</sub> as an example. The monolayer GO powders were added to 50 mL of deionized water, and the mixture was put into an ultrasonic cleaner and treated at 53 kHz for 6 h to obtain the monolayer GO solution. 1.56 mL of Pt(NO<sub>3</sub>)<sub>2</sub>·2H<sub>2</sub>O aqueous solution (0.004 mol/L) and 3 mg of PVA (Pt/PVA mass ratio = 1.5:1.0) were first added to 200 mL of deionized water at 0 °C (under ice–water bath condition), then the GO solution was added and stirred vigorously for 30 min. After that, a certain amount of NaBH<sub>4</sub> (GO/NaBH<sub>4</sub> mass ratio = 1:400) was added to the above mixture to generate a brown suspension, followed by further stirring for 60 min to obtain the Pt-rGO composite solution. About 1.0 g of the above synthesized  $\alpha$ -MnO<sub>2</sub> nanorods was added to the Pt-rGO composite solution and stirred for 6 h. The doped graphene oxide was transformed into the reduced GO (rGO) due to the use of NaBH<sub>4</sub>. After that, the samples were washed with deionized water and dried in an oven at 80 °C for 12 h. Finally, the samples were placed in a muffle furnace and the heating rate was adjusted to 3 °C/min to calcine the samples from RT to 400 °C and kept at this temperature for 2 h, thus obtaining the xPt-yrGO/ $\alpha$ -MnO<sub>2</sub> samples. In Table S2, the results of inductively coupled plasma–atomic emission spectroscopy (ICP–AES) characterization show that the actual Pt loadings of these samples were very similar ( $x = 0.91$ – $0.94$  wt%) and just slightly lower than their theoretical loadings. Furthermore, the actual rGO loadings ( $y$ ) were 0.5, 1.0, and 2.0 wt%, respectively.

### 3.2. Characterization

Physicochemical properties of the  $\alpha$ -MnO<sub>2</sub> and xPt-yrGO/ $\alpha$ -MnO<sub>2</sub> samples were determined using the techniques, such as X-ray diffraction (XRD), ICP–AES, thermogravimetry (TG) analysis, N<sub>2</sub> adsorption–desorption (BET), Fourier transform infrared spectroscopy (FTIR), transmission electron microscopy (TEM), high-angle annular dark-field scanning transmission electron microscopy (HAADF–STEM), scanning electron microscopy (SEM), element mappings, X-ray photoelectron spectroscopy (XPS), hydrogen temperature-programmed reduction (H<sub>2</sub>-TPR), oxygen temperature-programmed desorption (O<sub>2</sub>-TPD), and in situ diffuse reflectance infrared Fourier transform spectroscopy (in situ DRIFTS). The detailed determination procedures are provided in the ESI.

### 3.3. Catalytic Activity Measurement

A fixed-bed quartz tube microreactor and gas chromatograph were used to measure the benzene oxidation activities over the samples. About 50 mg (40–60 mesh) of quartz sand was thoroughly mixed with 50 mg of the catalyst sample (40–60 mesh), placed into a fixed-bed quartz tube microreactor (inner diameter = 4.0 mm), and pretreated at 400 °C in a nitrogen stream of 50 mL/min for 1 h. The reactant mixture consisted of 1000 ppm benzene + 20 vol% O<sub>2</sub> + N<sub>2</sub> (balance). The total flow rate was 50–200 mL/min, corresponding to a gas hourly space velocity (GHSV) of 60,000–240,000 mL/(g h). The reaction products were analyzed online by gas chromatograph (GC-7900, Techcomp) equipped with a flame ion detector (FID) for the analysis of organic products. Benzene conversion ( $X$ ), reaction rate ( $r$ ), and turnover frequencies (TOFs) were calculated according to the following equations:

$$X = \frac{c_{\text{inlet}} - c_{\text{outlet}}}{c_{\text{inlet}}} \times 100$$

$$r = \frac{c_{\text{inlet}} \times X}{m_{\text{cat}}}$$

$$\text{TOF} = \frac{X \times c_{\text{inlet}}}{n_s \times D}$$

where  $c_{\text{inlet}}$  and  $c_{\text{outlet}}$  are the concentration of benzene in inlet and outlet gas, respectively,  $m_{\text{cat}}$  is the mass of the catalyst (g),  $n_s$  is the number of active sites (mol), and  $D$  is the Pt dispersion on the surface of the catalyst. In addition,  $T_{10\%}$ ,  $T_{50\%}$ , and  $T_{90\%}$  are used to denote the temperatures required for the conversion to reach 10, 50, and 90%, respectively.

#### 4. Conclusions

In summary,  $\alpha$ -MnO<sub>2</sub> nanorods were synthesized by the hydrothermal method, and Pt/ $\alpha$ -MnO<sub>2</sub> and xPt-yrGO/ $\alpha$ -MnO<sub>2</sub> catalysts with Pt loadings of 0.91–0.95 wt% and surface areas of 37.9–40.7 m<sup>2</sup>/g were prepared using the PVA-protecting reduction method. The average particle sizes of Pt nanoparticles in Pt/ $\alpha$ -MnO<sub>2</sub> and xPt-yrGO/ $\alpha$ -MnO<sub>2</sub> were 2.7–3.2 nm. Among all of the samples, 0.94Pt-1.0rGO/ $\alpha$ -MnO<sub>2</sub> exhibited the highest catalytic performance, and the best sulfur dioxide resistance of 0.94Pt-1.0rGO/ $\alpha$ -MnO<sub>2</sub> was attributed to the fact that the loading of the appropriate amount of rGO enhances the SMSI between Pt and  $\alpha$ -MnO<sub>2</sub> and the O<sub>ads</sub> concentration, thus improving catalytic activity of the sample for benzene oxidation. The catalytic activity was negatively affected by water vapor, which was caused by the competitive adsorption of water vapor and benzene, and such a deactivation was reversible. A series of physicochemical characterization reveal that the decrease in catalytic activity of the 0.94Pt-1.0rGO/ $\alpha$ -MnO<sub>2</sub> sample in the presence of SO<sub>2</sub> was due to the formation of sulfate on the sample surface, which covered the active sites and oxygen vacancies. In addition, a possible oxidation mechanism was proposed as follows: (i) benzene is oxidized to phenolics by the reactive oxygen species; (ii) the generated phenolics are converted to benzoquinone or cyclohexanone; and (iii) the aromatic ring is destroyed to carboxylic acids, which are further oxidized to CO<sub>2</sub> and H<sub>2</sub>O. The strategy of enhancing the SMSI by loading of rGO is effective for designing new high-performance catalysts in the application of VOCs removal.

**Supplementary Materials:** The following supporting information can be downloaded at: <https://www.mdpi.com/article/10.3390/catal12111426/s1>. Figure S1: FTIR spectra of (a)  $\alpha$ -MnO<sub>2</sub>, (b) 0.93Pt/ $\alpha$ -MnO<sub>2</sub>, (c) 0.91Pt-0.5rGO/ $\alpha$ -MnO<sub>2</sub>, (d) 0.94Pt-1.0rGO/ $\alpha$ -MnO<sub>2</sub>, and (e) 0.92Pt-2.0rGO/ $\alpha$ -MnO<sub>2</sub>. Figure S2: (A) Nitrogen adsorption–desorption isotherms and (B) pore-size distributions of (a)  $\alpha$ -MnO<sub>2</sub>, (b) 0.93Pt/ $\alpha$ -MnO<sub>2</sub>, (c) 0.91Pt-0.5rGO/ $\alpha$ -MnO<sub>2</sub>, (d) 0.94Pt-1.0rGO/ $\alpha$ -MnO<sub>2</sub>, and (e) 0.92Pt-2.0rGO/ $\alpha$ -MnO<sub>2</sub>. Figure S3: Noble particle-size distributions of (a) 0.93Pt/ $\alpha$ -MnO<sub>2</sub>, (b) 0.91Pt-0.5rGO/ $\alpha$ -MnO<sub>2</sub>, (c) 0.94Pt-1.0rGO/ $\alpha$ -MnO<sub>2</sub>, and (d) 0.92Pt-2.0rGO/ $\alpha$ -MnO<sub>2</sub>. Figure S4: O<sub>2</sub>-TPD profiles of (a)  $\alpha$ -MnO<sub>2</sub>, (b) 0.93Pt/ $\alpha$ -MnO<sub>2</sub>, (c) 0.91Pt-0.5rGO/ $\alpha$ -MnO<sub>2</sub>, (d) 0.94Pt-1.0rGO/ $\alpha$ -MnO<sub>2</sub>, and (e) 0.92Pt-2.0rGO/ $\alpha$ -MnO<sub>2</sub>. Figure S5: Effect of benzene concentration on catalytic activity of 0.94Pt-1.0rGO/ $\alpha$ -MnO<sub>2</sub> at GHSV = 60,000 mL/(g h). Table S1: Comparison on specific reaction rates ( $r_{\text{cat}}$ ) for benzene oxidation at 160 °C over the catalysts studied in the present work and reported in the literature. Table S2: Average Pt particle sizes and actual Pt loadings of the as-obtained samples determined by the ICP–AES technique.

**Author Contributions:** Conceptualization, Q.Y.; methodology, D.Z.; software, D.Z.; investigation, D.Z.; resources, Q.Y.; data curation, D.Z., N.D., W.W. and Y.X.; writing—original draft preparation, D.Z.; writing—review and editing, Q.Y. and H.D.; visualization, D.Z., N.D., W.W. and Y.X.; supervision, Q.Y. and H.D.; project administration, Q.Y.; funding acquisition, Q.Y. All authors have read and agreed to the published version of the manuscript.

**Funding:** This work was supported by the National Natural Science Foundation of China (No. 21277008) and the National Key Research and Development Program of China (No. 2017YFC0209905).

**Data Availability Statement:** All the relevant data used in this study have been provided in the form of figures and tables in the published article, and all data provided in the present manuscript are available to whom they may concern.

**Conflicts of Interest:** The authors declare no conflict of interest.

## References

1. Kamal, M.S.; Razzak, S.A.; Hossain, M.M. Catalytic oxidation of volatile organic compounds (VOCs)—A review. *Atmos. Environ.* **2016**, *140*, 117–134. [[CrossRef](#)]
2. Zhao, Q.; Li, Y.; Chai, X.; Xu, L.; Zhang, L.; Ning, P.; Huang, J.; Tian, S. Interaction of inhalable volatile organic compounds and pulmonary surfactant: Potential hazards of VOCs exposure to lung. *J. Hazard. Mater.* **2019**, *369*, 512–520. [[CrossRef](#)] [[PubMed](#)]
3. He, C.; Cheng, J.; Zhang, X.; Douthwaite, M.; Pattison, S.; Hao, Z. Recent advances in the catalytic oxidation of volatile organic compounds: A review based on pollutant sorts and sources. *Chem. Rev.* **2019**, *119*, 4471–4568. [[CrossRef](#)] [[PubMed](#)]
4. Guo, J.; Lin, C.; Jiang, C.; Zhang, P. Review on noble metal-based catalysts for formaldehyde oxidation at room temperature. *Appl. Surf. Sci.* **2019**, *475*, 237–255. [[CrossRef](#)]
5. Dong, N.; Ye, Q.; Chen, M.; Cheng, S.; Kang, T.; Dai, H. Sodium-treated sepiolite-supported transition metal (Cu, Fe, Ni, Mn, or Co) catalysts for HCHO oxidation. *Chin. J. Catal.* **2020**, *41*, 1734–1744. [[CrossRef](#)]
6. Yi, H.; Song, L.; Tang, X.; Zhao, S.; Yang, Z.; Xie, X.; Ma, C.; Zhang, Y.; Zhang, X. Effect of microwave absorption properties and morphology of manganese dioxide on catalytic oxidation of toluene under microwave irradiation. *Ceram. Int.* **2020**, *46*, 3166–3176. [[CrossRef](#)]
7. Yang, W.; Su, Z.A.; Xu, Z.; Yang, W.; Peng, Y.; Li, J. Comparative study of  $\alpha$ -,  $\beta$ -,  $\gamma$ - and  $\delta$ -MnO<sub>2</sub> on toluene oxidation: Oxygen vacancies and reaction intermediates. *Appl. Catal. B* **2020**, *260*, 118150. [[CrossRef](#)]
8. Zeng, X.; Li, B.; Liu, R.; Li, X.; Zhu, T. Investigation of promotion effect of Cu doped MnO<sub>2</sub> catalysts on ketone-type VOCs degradation in a one-stage plasma-catalysis system. *Chem. Eng. J.* **2020**, *384*, 123362. [[CrossRef](#)]
9. Huang, F.; Wang, X.; Zhu, Q.; Li, K.; Zhou, X.; Lu, S.; Fan, Z.; He, L.; Liu, Y.; Pang, F. Efficient formaldehyde elimination over Ag/MnO<sub>2</sub> nanorods: Influence of the Ag loading. *Catal. Surv. Asia* **2019**, *23*, 33–40. [[CrossRef](#)]
10. Xie, S.; Liu, Y.; Deng, J.; Yang, J.; Zhao, X.; Han, Z.; Zhang, K.; Lu, Y.; Liu, F.; Dai, H. Carbon monoxide oxidation over rGO-mediated gold/cobalt oxide catalysts with strong metal-support interaction. *ACS Appl. Mater. Interfaces* **2020**, *12*, 31467–31476. [[CrossRef](#)]
11. Lu, L.; Tian, H.; He, J.; Yang, Q. Graphene–MnO<sub>2</sub> hybrid nanostructure as a new catalyst for formaldehyde oxidation. *J. Phys. Chem. C* **2016**, *120*, 23660–23668. [[CrossRef](#)]
12. Wu, S.; He, Q.; Zhou, C.; Qi, X.; Huang, X.; Yin, Z.; Yang, Y.; Zhang, H. Synthesis of Fe<sub>3</sub>O<sub>4</sub> and Pt nanoparticles on reduced graphene oxide and their use as a recyclable catalyst. *Nanoscale* **2012**, *4*, 2478. [[CrossRef](#)] [[PubMed](#)]
13. Liu, X.; Ding, S.; Shigenobu, S.; Hojo, H.; Einaga, H. Catalyst design of Pt/TiO<sub>2</sub> microsphere for benzene oxidation under microwave irradiation. *Catal. Today* **2021**, *376*, 285–291. [[CrossRef](#)]
14. Wu, B.; Chen, B.; Zhu, X.; Yu, L.; Shi, C. Lower loading of Pt on hydrophobic Ts-1 zeolite: A high-efficiency catalyst for benzene oxidation at low temperature. *Catal. Today* **2020**, *355*, 512–517. [[CrossRef](#)]
15. Guo, Y.; Sun, Y.; Yang, D.; Dai, J.; Liu, Z.; Chen, Y.; Huang, J.; Li, Q. Biogenic Pt/CaCO<sub>3</sub> nanocomposite as a robust catalyst toward benzene oxidation. *ACS Appl. Mater. Interfaces* **2020**, *12*, 2469–2480. [[CrossRef](#)]
16. Hao, X.; Dai, L.; Deng, J.; Liu, Y.; Jing, L.; Wang, J.; Pei, W.; Zhang, X.; Hou, Z.; Dai, H. Nanotubular OMS-2 supported single-atom platinum catalysts highly active for benzene oxidation. *J. Phys. Chem. C* **2021**, *125*, 17696–17708. [[CrossRef](#)]
17. Yang, K.; Liu, Y.; Deng, J.; Zhao, X.; Yang, J.; Han, Z.; Hou, Z.; Dai, H. Three-dimensionally ordered mesoporous iron oxide-supported single-atom platinum: Highly active catalysts for benzene combustion. *Appl. Catal. B* **2019**, *244*, 650–659. [[CrossRef](#)]
18. Zheng, J.; Wang, Z.; Chen, Z.; Zuo, S. Mechanism of CeO<sub>2</sub> synthesized by thermal decomposition of Ce-MOF and its performance of benzene catalytic combustion. *J. Rare Earths* **2021**, *39*, 790–796. [[CrossRef](#)]
19. Mori, K.; Shimada, M.; Horiuchi, Y.; Ohmichi, T.; Nishiyama, N.; Fujii, H.; Yamashita, H. Preparation of nano-sized Pt metal particles by photo-assisted deposition (PAD) on transparent Ti-containing mesoporous silica thin film. *Res. Chem. Intermed.* **2008**, *34*, 495–505. [[CrossRef](#)]
20. Zhang, K.; Dai, L.; Liu, Y.; Deng, J.; Jing, L.; Zhang, K.; Hou, Z.; Zhang, X.; Wang, J.; Feng, Y.; et al. Insights into the active sites of chlorine-resistant Pt-based bimetallic catalysts for benzene oxidation. *Appl. Catal. B* **2020**, *279*, 119372. [[CrossRef](#)]
21. Chen, Z.; Mao, J.; Zhou, R. Preparation of size-controlled Pt supported on Al<sub>2</sub>O<sub>3</sub> nanocatalysts for deep catalytic oxidation of benzene at lower temperature. *Appl. Surf. Sci.* **2019**, *465*, 15–22. [[CrossRef](#)]
22. Xia, Y.; Xia, L.; Liu, Y.; Yang, T.; Deng, J.; Dai, H. Concurrent catalytic removal of typical volatile organic compound mixtures over Au–Pd/ $\alpha$ -MnO<sub>2</sub> nanotubes. *J. Environ. Sci.* **2018**, *64*, 276–288. [[CrossRef](#)] [[PubMed](#)]
23. Cheng, L.; Wang, J.; Zhang, C.; Jin, B.; Men, Y. Boosting acetone oxidation efficiency over MnO<sub>2</sub> nanorods by tailoring crystal phases. *New J. Chem.* **2019**, *43*, 19126–19136. [[CrossRef](#)]
24. Chen, D.; Zhang, G.; Wang, M.; Li, N.; Xu, Q.; Li, H.; He, J.; Lu, J. Pt/MnO<sub>2</sub> nanoflowers anchored to boron nitride aerogels for highly efficient enrichment and catalytic oxidation of formaldehyde at room temperature. *Angew. Chem. Int. Ed.* **2021**, *60*, 6377–6381. [[CrossRef](#)] [[PubMed](#)]
25. Wang, C.; Wang, H.; Zhai, C.; Ren, F.; Zhu, M.; Yang, P.; Du, Y. Three-dimensional Au<sub>0.5</sub>/reduced graphene oxide/carbon fiber electrode and its high catalytic performance toward ethanol electrooxidation in alkaline media. *J. Mater. Chem. A* **2015**, *3*, 4389–4398. [[CrossRef](#)]

26. Qin, Y.; Wang, Y.; Li, J.; Qu, Z. Effect of Ag on toluene oxidation over Ag supported wire-like MnO<sub>2</sub> catalysts. *Surf. Interf.* **2020**, *21*, 100657. [[CrossRef](#)]
27. Zhang, L.; Zhu, S.; Li, R.; Deng, W.; Hong, C.; Liu, D.; Guo, L. Ag-doped  $\delta$ -MnO<sub>2</sub> nanosheets as robust catalysts for toluene combustion. *ACS Appl. Nano Mater.* **2020**, *3*, 11869–11880. [[CrossRef](#)]
28. Lu, S.; Zhu, Q.; Dong, Y.; Zheng, Y.; Wang, X.; Li, K.; Huang, F.; Peng, B.; Chen, Y. Influence of MnO<sub>2</sub> morphology on the catalytic performance of Ag/MnO<sub>2</sub> for the HCHO oxidation. *Catal. Surv. Asia* **2019**, *23*, 210–218. [[CrossRef](#)]
29. Wang, Y.; Liu, H.; Wang, S.; Luo, M.; Lu, J. Remarkable enhancement of dichloromethane oxidation over potassium-promoted Pt/Al<sub>2</sub>O<sub>3</sub> catalysts. *J. Catal.* **2014**, *311*, 314–324. [[CrossRef](#)]
30. Wang, Y.; Wang, G.; Deng, W.; Han, J.; Qin, L.; Zhao, B.; Guo, L.; Xing, F. Study on the structure-activity relationship of Fe-Mn oxide catalysts for chlorobenzene catalytic combustion. *Chem. Eng. J.* **2020**, *395*, 125172. [[CrossRef](#)]
31. Yan, Z.; Xu, Z.; Yang, Z.; Yue, L.; Huang, L. Graphene oxide/Fe<sub>2</sub>O<sub>3</sub> nanoplates supported Pt for enhanced room-temperature oxidation of formaldehyde. *Appl. Surf. Sci.* **2019**, *467–468*, 277–285. [[CrossRef](#)]
32. Yashnik, S.A.; Chesalov, Y.A.; Ishchenko, A.V.; Kaichev, V.V.; Ismagilov, Z.R. Effect of Pt addition on sulfur dioxide and water vapor tolerance of Pd-Mn-hexaaluminate catalysts for high-temperature oxidation of methane. *Appl. Catal. B* **2017**, *204*, 89–106. [[CrossRef](#)]
33. Sun, P.; Long, Y.; Long, Y.; Cao, S.; Weng, X.; Wu, Z. Deactivation effects of Pb(ii) and sulfur dioxide on a  $\gamma$ -MnO<sub>2</sub> catalyst for combustion of chlorobenzene. *J. Colloid Interf. Sci.* **2020**, *559*, 96–104. [[CrossRef](#)] [[PubMed](#)]
34. Chen, Y.W.; Li, B.; Niu, Q.; Li, L.; Kan, J.W.; Zhu, S.M.; Shen, S.B. Combined promoting effects of low-Pd-containing and Cu-doped LaCoO<sub>3</sub> perovskite supported on cordierite for the catalytic combustion of benzene. *Environ. Sci. Pollut. Res.* **2016**, *23*, 15193–15201. [[CrossRef](#)] [[PubMed](#)]
35. Wu, P.; Zhao, S.; Yu, J.; Jin, X.; Ye, D.; Yang, S.; Qiu, Y. Effect of absorbed sulfate poisoning on the performance of catalytic oxidation of VOCs over MnO<sub>2</sub>. *ACS Appl. Mater. Interfaces* **2020**, *12*, 50566–50572. [[CrossRef](#)]
36. Wilburn, M.S.; Epling, W.S. SO<sub>2</sub> adsorption and desorption characteristics of Pd and Pt catalysts: Precious metal crystallite size dependence. *Appl. Catal. A* **2017**, *534*, 85–93. [[CrossRef](#)]
37. Li, J.; Cai, S.; Yu, E.; Weng, B.; Chen, X.; Chen, J.; Jia, H.; Xu, Y. Efficient infrared light promoted degradation of volatile organic compounds over photo-thermal responsive Pt-rGO-TiO<sub>2</sub> composites. *Appl. Catal. B* **2018**, *233*, 260–271. [[CrossRef](#)]
38. Rong, S.; Zhang, P.; Liu, F.; Yang, Y. Engineering crystal facet of  $\alpha$ -MnO<sub>2</sub> nanowire for highly efficient catalytic oxidation of carcinogenic airborne formaldehyde. *ACS Catal.* **2018**, *8*, 3435–3446. [[CrossRef](#)]
39. Wu, X.; Lee, H.; Liu, S.; Weng, D. Sulfur poisoning and regeneration of MnO<sub>x</sub>-CeO<sub>2</sub>-Al<sub>2</sub>O<sub>3</sub> catalyst for soot oxidation. *J. Rare Earths* **2012**, *30*, 659–664. [[CrossRef](#)]
40. Wang, X.; Liu, Y.; Zhang, T.; Luo, Y.; Lan, Z.; Zhang, K.; Zuo, J.; Jiang, L.; Wang, R. Geometrical-site-dependent catalytic activity of ordered mesoporous Co-based spinel for benzene oxidation: In situ Drifts study coupled with Raman and EXAFS spectroscopy. *ACS Catal.* **2017**, *7*, 1626–1636. [[CrossRef](#)]
41. Sivasankar, N.; Vasudevan, S. Temperature-programmed desorption and infrared spectroscopic studies of benzene adsorption in zeolite ZSM-5. *J. Phys. Chem. B* **2004**, *108*, 11585–11590. [[CrossRef](#)]
42. Wang, X.; Zhao, W.; Wu, X.; Zhang, T.; Liu, Y.; Zhang, K.; Xiao, Y.; Jiang, L. Total oxidation of benzene over ACo<sub>2</sub>O<sub>4</sub> (A = Cu, Ni and Mn) catalysts: In situ drifts account for understanding the reaction mechanism. *Appl. Surf. Sci.* **2017**, *426*, 1198–1205. [[CrossRef](#)]
43. Ma, X.; Xiao, M.; Yang, X.; Yu, X.; Ge, M. Boosting benzene combustion by engineering oxygen vacancy-mediated Ag/CeO<sub>2</sub>-Co<sub>3</sub>O<sub>4</sub> catalyst via interfacial electron transfer. *J. Colloid Interf. Sci.* **2021**, *594*, 882–890. [[CrossRef](#)]
44. Li, Z.; Yang, D.; Chen, Y.; Du, Z.; Guo, Y.; Huang, J.; Li, Q. Waste eggshells to valuable CO<sub>3</sub>O<sub>4</sub>/CaCO<sub>3</sub> materials as efficient catalysts for VOCs oxidation. *Mol. Catal.* **2020**, *483*, 110766. [[CrossRef](#)]
45. Zhao, X.; Xu, D.; Wang, Y.; Zheng, Z.; Li, K.; Zhang, Y.; Zhan, R.; Lin, H. Electric field assisted benzene oxidation over Pt-Ce-Zr nano-catalysts at low temperature. *J. Hazard. Mater.* **2021**, *407*, 124349. [[CrossRef](#)]
46. Li, L.; Yang, Q.; Wang, D.; Peng, Y.; Yan, J.; Li, J.; Crittenden, J. Facile synthesis  $\lambda$ -MnO<sub>2</sub> spinel for highly effective catalytic oxidation of benzene. *Chem. Eng. J.* **2021**, *421*, 127828. [[CrossRef](#)]
47. Wang, Z.; Yang, H.; Liu, R.; Xie, S.; Liu, Y.; Dai, H.; Huang, H.; Deng, J. Probing toluene catalytic removal mechanism over supported Pt nano- and single-atom-catalyst. *J. Hazard. Mater.* **2020**, *392*, 122258. [[CrossRef](#)] [[PubMed](#)]
48. He, D.; Jiang, Y.; Lv, H.; Pan, M.; Mu, S. Nitrogen-doped reduced graphene oxide supports for noble metal catalysts with greatly enhanced activity and stability. *Appl. Catal. B* **2013**, *132–133*, 379–388. [[CrossRef](#)]
49. Mady, A.H.; Baynosa, M.L.; Tuma, D.; Shim, J. Facile microwave-assisted green synthesis of Ag-ZnFe<sub>2</sub>O<sub>4</sub>@rGO nanocomposites for efficient removal of organic dyes under UV- and visible-light irradiation. *Appl. Catal. B* **2017**, *203*, 416–427. [[CrossRef](#)]